QATAR UNIVERSITY

COLLEGE OF ARTS AND SCIENCES

RATIONAL DESIGN OF MXENES WITH ATOMICALLY DOPED MULTIMETALS FOR EFFICIENT ELECTROCHEMICAL AND PHOTOELECROCHEMICAL CONVERSION OF CO2 TO USABLE HYDROCARBONS

BY

YASSEEN S. IBRAHIM

A Thesis Submitted to

the College of Arts and Sciences

in Partial Fulfillment of the Requirements for the Degree of

Masters of Science in Material Science and Technology

June 2021

COMMITTEE PAGE

The members of the Committee approve the Thesis of
YASSEEN S. IBRAHIM defended on 28/04/2021.

Ahmed Elzatahry
Thesis/Dissertation Supervisor

Aboubakr Abdullah
Committee Member

Talal Altahtamouni
Committee Member

Mohamed Hassan
Committee Member

Kamel Eid
Committee Member

Approved:

Ibrahim AlKaabi, Dean, College of Arts and Sciences

ABSTRACT

IBRAHIM, YASSEEN, S., Masters:June:[2021]:, Material Science and Technology

Title: Rational design of MXenes with atomically doped multimetals for efficient electrochemical and photoelectrochemical conversion of CO_2 to usable hydrocarbons

Supervisor of Thesis: Ahmed A. Elzatahry.

Ti_3C_2Tx MXene is a promising catalyst for several applications; however, its electrochemical conversion of CO_2 to useable hydrocarbons has been rarely reported experimentally. Herein, two-dimensional $Ti_3C_2T_x$ nanosheets doped at an atomic level with Pd-M/$Ti_3C_2T_x$ (M: Cu and Co) were synthesized by etching off the Al atom in Ti_3AlC_2 followed by intercalation and exfoliation. Thereafter, Pd-Cu and Pd-Co were doped in $Ti_3C_2T_x$ nanosheets. The fabrication method is based on creating Tx group upon etching along with highly active Ti vacancies that are ideal sites for anchoring and stabilizing the doped metal atoms. The electrochemical CO_2RR (CO_2 reduction reaction) for the fabricated sample Pd-Cu/$Ti_3C_2T_x$ and Pd-Co/$Ti_3C_2T_x$ resulted in converting CO_2 into α-Glucose and formate ($HCOO^-$), respectively. The CO_2RR current density of Pd-Cu/$Ti_3C_2T_x$ (0.66 $mAcm^{-2}$) was the highest compared to the rest of the doped samples and more than 3 times that of pristine MXene $Ti_3C_2T_x$ (0.18 $mAcm^{-2}$). The as-synthesized Pd-M/$Ti_3C_2T_x$ combine between the unique catalytic merits of two dopants and quick charge transfer and electron density of $Ti_3C_2T_x$. This study may pave perspectives on the development of MXenes for CO_2RR to valuable fuels.

TABLE OF CONTENTS

LIST OF FIGURES

CHAPTER 1: INTRODUCTION

The depleting of fossil energy resources is not only looming but also releasing notorious CO_2 that causes global warming and air pollution.[1-5] The electrochemical CO_2RR is an intriguing approach for decarbonization of energy economy, manufacture of renewable fuels, or valuable chemicals; however, CO_2RR selectivity, cost, and productivity remain daunting challenges.[1-4, 6-11] Various electrocatalysts such as noble metals (i.e., Pt, Pd, Ag, and Au), transition metals (i.e., Fe, Bi, and Ti), carbon-based (i.e., carbon nitride and graphene oxide), and hybrid electrocatalysts were developed for CO_2RR to various chemicals [9, 12-15], since the early work is done for CO_2RR using Cu electrode to form CO, CH_4, and C_2H_4.[6, 16] HCOOH is a highly desired CO_2RR product, as its importance in various end-use industries as pharmaceuticals, hydrogen generation, rubber, and pesticides, so the global market of HCOOH exceeded 750 $ million in 2019.[17, 18] various transition metals showed high selectivity towards COOH, such as Hg, In, Sn, Cd, Bi, and Tl.[19, 20] Pd-Cu or Pd-Co together are among the most active CO_2RR electrocatalyst due to their inherent catalytic merits, d-electron availability, low surface CO_2 adsorption strengths, and modulated chemisorption strengths of the CO_2RR intermediates ($CO_2\bullet^{-}$and $CO\bullet$) allowing the reduction of CO_2 to HCOOH and other valuable multi-carbon products. [6, 10, 21-35] Also, Pd-M can easily protonate the adsorbed CO_2 to form adsorbed OCHO intermediate, which can easily be transformed into formic or other hydrocarbons.[36] Pd/M reduces the adsorption strength of intermediates like $CO2\bullet^{-}$ anion radical and $CO\bullet$ radical to allow the selective formation of HCOOH.[36] Pd/M can inhibit the hydrogen evolution reaction (HER) owing to the low activity of Pd toward the HER; meanwhile, Cu, with its high conductivity, enhance mass transport, especially at high reaction rates.[37-39]

Using another cocatalyst, especially $Ti_3C_2T_x$ MXene with Pd-Cu or Pd-Co, can be an effective way for further improvement CO_2RR fundamentally (i.e., activity and selectivity) and practically (i.e., mass transport, product rate/yield, and energy efficiency) due to the two-dimensional, multilayered structure, high conductivity, beside the unique composition including (C with Ti, and surface terminations T_X), which can tune the binding configuration and stabilization of intermediates with different scaling relations. [40-53] Also, $Ti_3C_2T_x$ can alternating -C-coordinated intermediates (e. g., *COOH, *CHO) as fragments and −H-coordinated intermediates (e. g., *HCOOH, *H_2CO) as complete molecules that decouples scaling relations. [53] The utilization of $Ti_3C_2T_x$ in CO_2RR was primarily based on theoretical calculations, although some rare works on CO_2RR experimentally.[41-57] For instance, Ti_3C_2/g-C_3N_4 enhanced the CO_2RR to formate and methanol by 10 times higher than g-C_3N_4 catalyst.[58] The CO_2RR to methanol on Ti_3C_2 quantum dots/Cu_2O nanowires was 8.25 and 2.15 times that of Cu_2O NWs/Cu and Ti_3C_2 sheets/Cu_2O, respectively.[59] Ti_2CT_x reduced CO_2 to HCOOH as the main product with a FE over 56.1 % at -1.8 V, and T_X groups play an essential role in enhancement CO_2RR.[60] Thus, the combination between Pd dopants and Ti_3C_2Tx can enhance CO_2RR selectivity to HCOOH or C_2 which was not yet reported.

Here, 2D $Ti_3C_2T_x$ (T_x = O, OH, and F) nanosheets co-doped atomically with Pd-M, where M is Cu and Co (denoted as Pd-Cu/$Ti_3C_2T_x$ and Pd-Co/$Ti_3C_2T_x$) were synthesized for the sake of enhancement the CO_2RR. Unlike previous reports, the as-synthesized Pd-M/$Ti_3C_2T_x$ combine between the unique catalytic merits of two dopants (i.e., synergistic effect, selectivity, optimal intermediates binding, and inferior H_2 production) and intrinsic properties of $Ti_3C_2T_x$ (i.e., conductivity, defects, abundantly exposed surface atoms, layered structure which promotes chemisorption of reactants and enhancing catalytic performance). Also, $Ti_3C_2T_x$ provides abundant Ti-deficit vacancies with a high reduction ability, which can accommodate the binary dopants and stabilize them against aggregation. The as-obtained doped Mxene nanosheets are dispersable as ink in various solvents to be coated onto powder, sheets, films to form electrodes by simple casting or spin coating or a vacuum drying at room temperature. The electrochemical CO_2RR activity and stability of Pd-M/$Ti_3C_2T_x$ were benchmarked compared to Pd/$Ti_3C_2T_x$, Cu/$Ti_3C_2T_x$, Co/$Ti_3C_2T_x$, and pristine $Ti_3C_2T_x$. The CO2RR mechanism was investigated by various reaction experiments and characterization tools.

CHAPTER 2: LITERATURE REVIEW

Ever since the industrial revolution and the emission of greenhouse gasses such as CO_2 have been increasing dramatically due to the rapid growth of industry and the consumption of fossil fuels (ex: natural gas, petroleum, and coal), resulting in an environmental and energy dilemma.[61-65] As a result, several researchers have been published on the photoconversion of $CO_{2,}$ specifically reduction into hydrocarbons such as methane[66], methanol[67], formic acid[67], formaldehyde[68], as a promising and economical method to solve both the energy insufficiency and environmental issues. Yet, the developed catalysts still didn't meet the market standards as they fall short in charge-carrier separation and transfer, spontaneous adsorption for CO_2, active surface sites, and a delay in the recombination of the excited electrons, such as Cds[69, 70], g-C_3N_4.[71] One of the effective approaches to overcome these issues is to use a composite catalyst by introducing a co-catalyst[72], especially noble metals such as Pt/Cu[73], Pt[74], Au[75], Ag.[76] Even though noble metals as cocatalysts boost the performance of photocatalysts, the expensive cost and scarcity limit their usage.

MXene is one of the recently discovered materials.[77] that has been attracting attention as it has been used in various applications.[78-83] MXenes (Mn+1Xn) are fabricated by selective chemical etching of A layer from the MAX phase. M is a transition metal, A is an element from group 3A or 4A, X is either carbon or nitrogen, and n is an integer number (1-4). the wide use of MXene compounds is owned to their outstanding electric conductivity, surface-active sites, a photothermal conversion that improves the catalyst activity and promotes the reaction rate.[84-86]

In the last 10 years, MXenes sparked researchers in different fields ranging from catalysis to biomedical. The following section highlights the recent advances made in the controlled fabrication of MXenes for CO_2 reduction supported with various examples and related results. In this chapter, the photocatalytic reduction of CO_2 is studied using MXene as a cocatalyst, exploring the fabrication methods, characterization, and photocatalytic performance and the MXene role in the process. Moreover, this study will certainly open the door for new fabrication methods for the MXene based composites that will greatly influence the photocatalytic performance.

For example, a novel 2D/2D heterojunction of ultrathin Ti_3C_2/Bi_2WO_6 nanosheets was designed[54], as shown in Fig. 2.1a. The aluminum was chemically removed from the MAX phase by hydrofluoric acid, forming a multilayer of MXene. Subsequently, the etched MXene was intercalated using dimethyl sulfoxide (DMSO) then exfoliated to form Ti_3C_2 nanosheets. One after the other, Bismuth (III) nitrate and Sodium tungstate-CTAB solutions were added to the MXene nanosheets undergoing a hydrothermal reaction to form the 2D/2D structure of Ti_3C_2/Bi_2WO_6. Such a usage of the unique 2D structure of MXene favors the fabrication of a 2D/2D heterostructure over its counterparts forming 0D/2D and 1D/2D, endowing strong surface connection between the cocatalyst (MXene) and the photocatalyst (Bi_2WO_6) and further assures better stability.[87] The intimate contact formation within the 2D/2D heterojunction further enhances the transfer and separation of induced charge carriers. Owning to a crucial factor as strong physical and electronic coupling effect that enhances the photocatalytic efficiency, despite the decrease in surface area due to the stacking of the nanosheets. Charge transfer dynamics examinations were performed, such as electrochemical impedance spectra (EIS) and transient photocurrent response, to set forth the difference in charge transfer capability between

TB0 and TB2 (0% and 2% mass ratio of Ti_3C_2 to Bi_2WO_6).[54]

EIS plot Fig. 2.1b shows TB2 having a lower charge transfer resistance compared to TB0, represented as the shorter arc. Whereas the transient photocurrent response, as demonstrated in Fig. 2.1c, shows a higher current density for TB2 over TB0, as well as the insignificant photocurrent performance of Ti_3C_2, proving that the Ti_3C_2 essential part is to accept electrons for subsequent catalytic reactions and the Bi2WO6 in Ti_3C_2/Bi_2WO_6, is the one responsible for the generation of the photo-induced electrons. The photocatalytic performance for CO_2 reduction of the prepared samples were analyzed in a solar irradiation simulated medium. Both methane and methanol were the major photocatalytic products with a higher selectivity for methane[54], as shown in Fig2.1 d. The most optimum sample TB2 (2% mass ratio of Ti_3C_2 to Bi_2WO_6) shows a conversion rate of 1.7 µmol. g-1.h-1 for CH_4 and 0.44 µmol. g-1.h-1 CH_3OH representing four and six folds of methane and methanol, respectively, compared with pristine Bi_2WO_6. The boosted photocatalytic behavior of the Ti_3C_2/Bi_2WO_6 hybrid is ascribed to the fast charge transfer from Bi_2WO_6 to the surface of Ti_3C_2, the increase in the surface area upon the incorporation of Ti_3C_2 with Bi_2WO_6, and the photothermal effect of Ti_3C_2, which activates the catalyst.[54]

Surface alkalinized MXene (Ti_3C_2OH) was coupled with commercial Titania (P25) via facile mechanical mixing. Ti_3C_2 powder was dispersed in KOH solution to substitute -F bond with -OH, taking advantage of the low stability of Ti-F bonds in basic solution.[88] Such a surface modification for MXenes was previously studied and demonstrated its potential in hydrogen evolution reaction. The gas evolution rate was compared for different samples to optimize the MXene content (wt%), catalyst or photocatalyst terminal surface group (-OH), and finally, compare the optimized result with other co-catalysts.

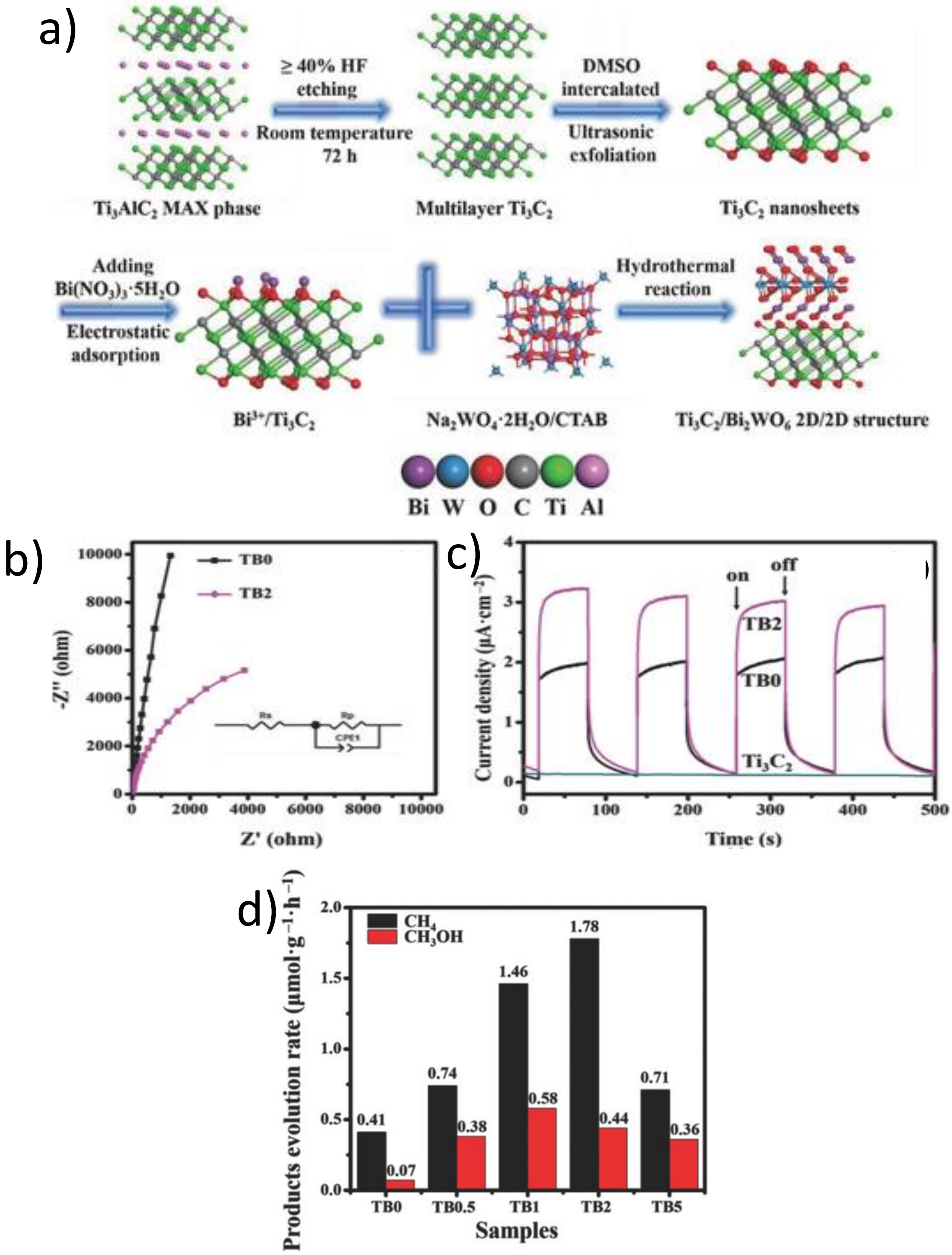

Figure 2.1: (a) Scheme of the fabrication process of Ti_3C_2/Bi_2WO_6 nanosheets. b) EIS comparison plot of Ti_3C_2 and Ti_3C_2/Bi_2WO_6 and c) transient photocurrent of the prepared samples. d) Photocatalytic activity of the fabricated samples.[54]

Based on the results (Fig 2.2a), 5 wt% of MXene coupled with P25 (5TC/P25) showed the highest rate conversion of CO_2 forming 3-fold (12.6 µmol g-1 h -1) of CO and 27-fold (1.6 µmol g-1 h -1) of CH_4 compared to pristine P25.[88] Increasing the load % of MXene any further would decrease the conversion rate resulted in blocking the light irradiation from the photocatalyst P25. Signifying the effectiveness of MXene as a co-catalyst in photocatalytic reduction upon optimizing its load. Thereby, the alkalization treatment was performed on the optimized loaded MXene sample to study the role effect of -OH on the surface of both the MXene and P25. The alkalinized co-catalyst (5TC-OH/P25) sample showed the highest conversion activity Fig2.2b, where the evolution rates of CO and CH_4 were 3-fold (11.74 µmol g-1 h -1) and 277-fold (16.61 µmol g-1 h -1) of the bare P25, respectively. In contrast with the non-alkylated hybrids, the rest of the hydroxy-decorated hybrids, and other catalysts (Fig2.2c), 5TC-OH/P25 showed selectivity for CH_4 evolution over CO. Yet, Ti_3C_2-OH didn't show any photoactivity for the CO_2 reduction. This confirms the P25 is the catalyst accountable for the photoreduction of CO_2 and that the sole rule of alkalization of Ti_3C_2 coupled with P25 is to influence the photocatalytic activity and the product selectivity in line with other reports.[89, 90] Furthermore, acidic molecules such as CO_2 are commonly adsorbed by basic sites.[91] The transient photocurrent (Fig. 2.2d) illustrates the higher response for 5TC/P25 and 5TC-P25 over the pristine P25, confirming the reinforcement of charge-carrier separation. The impedance spectroscopy (Fig. 2.2e) unravels the charge transfer enhancement of 5TC-OH/P25 represented with the smallest resistance.[88]

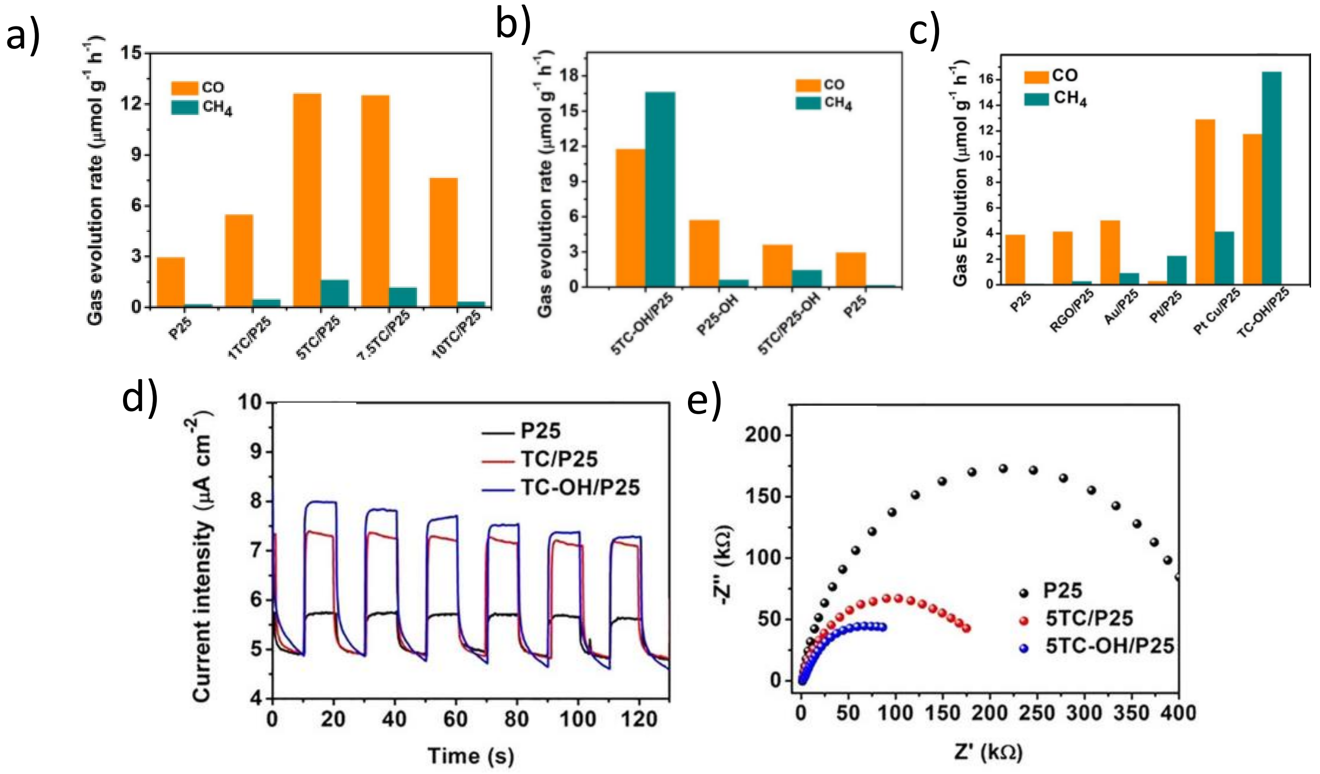

Figure 2.2: Gas evolution rates of CO and CH4 for different samples (a-c). d) Photo-current responses and e) EIS Nyquist plots.[88]

In-Situ Growth of TiO_2 NPs grafted on the conductive surface of Ti_3C_2 was prepared via a fictile calcination method, allowing for a better intimate contact area compared to mechanically mixed materials.[43] The mass loading of TiO_2 NPs was tailored by variating the calcination temperature at 0, 350, 450, 550, and 650 °C forming TT350, TT450, TT550, and TT650 samples, respectively. Confirmed by XRD (Fig. 2.3a), new diffraction peaks were found after calcination and intensified upon the increase of the calcination temperature, confirming the formation of TiO_2. On the other hand, at a magnified XRD (Fig. 2.3b), diffraction peaks of Ti_3C_2 located at 35° and 43° found to be damped with increasing the calcination temperature, owing to the transformation of Ti_3C_2 to TiO_2, especially for TT650 sample where the peaks are demolished.[43] More importantly, the uniform size distribution of TiO_2 nanoparticles is shown by SEM, forming a unique rice crust-like structure that is owned to the in-situ transformation of TiO_2 to Ti3C_2 that can restrain the agglomeration and maintain this uniformity (Fig. 2.3c).

Additionally, many air voids were found to be excited on TT550 due to the formation of CO_2 in the calcination step. However, the size of the air voids was decreasing upon further increasing the calcination temperature (increasing TiO_2 content) since the particle size will be larger, in line with the specific surface area. Such behavior is attributed to a trade-off relation between crystallinity and particle size. The TEM shows a sandwich-like of the formed TT550 sample, elucidating the transformation of Ti_3C_2 to TiO_2 is widespread from the surface, deep to the core (Fig. 2.3d). The intimate contact between TiO_2 NPs and Ti_3C_2 illustrated in the hetero-sandwich structure would result in a higher charge transfer.[43] The photocatalytic reduction of CO_2 for TiO_2/Ti_2C_3 composite was performed under the light. Among the three products, CH_4 was the most dominant product as it has the lowest reduction potential (-0.24 V) compared to CH_3OH (-0.38 V) and C_2H_5OH (-0.33 V). The general trend of methane production rate indicates improved performance upon increasing the calcination temperature till 550 °C. A deteriorated photocatalytic performance for TT650 owned to the non-attendance of Ti_3C_2, causing fast electron-hole recombination as well as a decrease in the surface area.[43] The best sample TT550 showed a production rate (0.22 µmol h -1) 3.7 times higher than the commercial catalyst TiO2 (P25) without explicit change production after 5 cycles (Fig. 2.3e,f).

Moreover, the obtained results are comparable with previous reports.[92-99] The enhanced photocatalytic reduction of CO_2 mechanism for TiO_2/Ti_3C_2 composite is owned to first, the increase in specific surface area enduing abundant active sites that promote the adsorption of CO_2. Second, the photothermal effect is generated by the adsorption of light from the inherent black color of Ti_3C_2. Third, the in-situ growth of TiO_2 of the surface of Ti_3C_2 generating a heterogeneous interface that alters the properties of pristine materials.[43]

A heterostructure was designed from 1D photoactive semiconductor (Cu2O nanowires (NWs)) and 0D MXene quantum dot (Ti_3C_2 QD) through an electrostatic self-assembly mechanism to enhance the photocatalytic reduction of CO_2.[59] Ti_3C_2 QD exhibits featured properties such as bandgap broadening as a result of quantum confinement, superior tunability in physicochemical properties, more active sites, and better dispersibility. A typical preparation of Ti_3C_2 using HF followed by a hydrothermal cutting for the Ti_3C_2 sheets forming Ti_3C_2 QD as shown in (Fig. 2.4a). Meanwhile, copper (Cu) mesh went through an anodization and calcination process, forming porous-Cu2O NWs/Cu. The electrostatic self-assembly of Ti_3C_2 QDs/Cu_2O NWs/Cu heterostructure is formed by tuning the surface charge of each Ti_3C_2 QDs and Cu_2O NWs/Cu with positive and negative charge using polyethyleneimine (PEI) and adding poly (sodium 4-styrene sulfonate) (PSS), respectively.[59] A porous surface structure of Cu_2O NWs was confirmed by FE-SEM (Fig. 2.4b). Whereas, Fig. 2.4c,d shows the conjunction rule of Ti_3C_2 QD and Ti_3C_2 sheets covering the porous surface while maintaining the overall structure of Cu_2O NWs. Three samples were prepared named Ti_3C_2 QDs/Cu_2O NWs/Cu, Ti_3C_2 sheet/Cu_2O NWs/Cu, and Cu_2O NWs/Cu to evaluate their performance in a photocatalytic reduction for CO_2. The three Cu_2O-based photocatalysts exhibit a selective conversion for methanol (CH_3OH) for 6 hours. Out of the prepared samples, Ti_3C_2 QDs/Cu_2O NWs/Cu stands with the highest yield of conversion (153.38 ppm cm^{-2}), which is 2.15 and 8.25 times its counterpart (70.25 ppm cm^{-2}) and pristine (18.82 ppm cm^{-2}) catalyst, respectively (Fig. 2.4e).

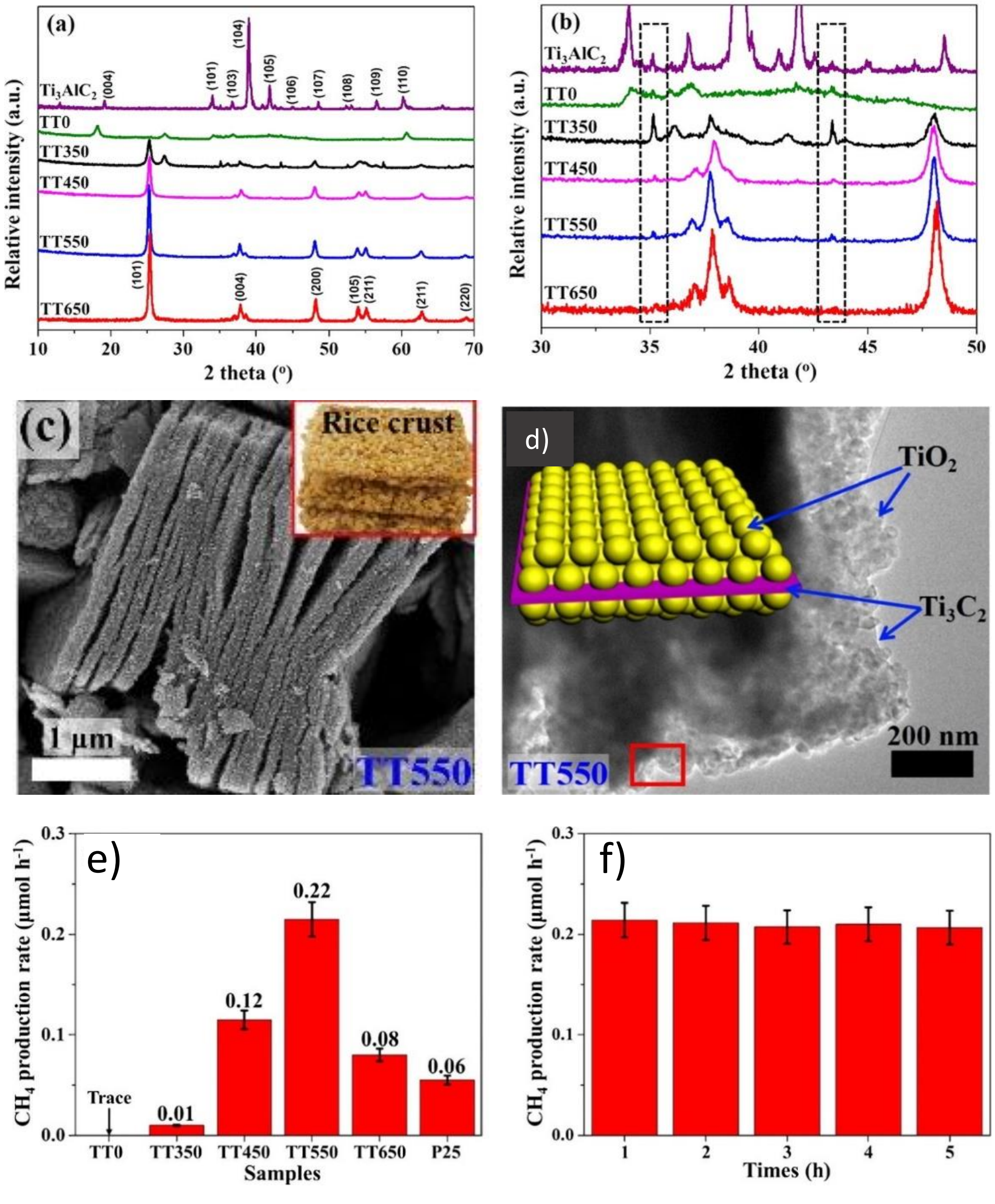

Figure 2.3: a) X-ray diffraction (XRD) and (b) magnified XRD for the hybrid samples with different content of MXene. c) FESEM image of TT550, d) TEM picture with a model of the sandwich structure of TT550. e) Photocatalytic performance for CH_4 production. f) stability test of TT550.[43]

The variation in conversion rate between the samples is ascribed to the small bandgap of Ti_3C_2 QDs/Cu_2O NWs/Cu over the other samples, enhancing UV-vis absorption and maximizing its utilization, delay electron-hole recombination and increase the photocatalytic performance, suggesting higher light adsorption.[59]

Additionally, the boost conversion upon the incorporation of Ti_3C_2 QD with the easily oxidized Cu_2O NWs asserts the protective aspect of Ti_3C_2 and that the QDs have more intimate contact with Cu2O than the sheets of Ti_3C_2. However, increasing the concentration of Ti_3C_2 QD above 0.5 mg/ml would block the catalyst's light adsorption, resulting in a decrease in the yield and photocurrent density. Similarly, the electrochemical impedance spectroscopy (EIS) displays the charge transfer resistance with the smallest semicircle for the Ti_3C_2 QDs/Cu_2O NWs/Cu suggesting a huge charge transfer enhancement.[59] The CO_2 conversion into methanol mechanism under solar light irradiation was proposed to be a 6-electron-transfer process. The electrons in Cu_2O valence band (VB) (1.497 V VS NHE) are photoexcited and accumulate at the fermi level (E_f)of Ti_3C_2 QD (-0.523 V) since Cu_2O conduction band (CB) (-0.703 V VS NHE) has a higher negative value than the E_f of Ti_3C_2 QD (Fig. 2.4f). The accumulated electrons catalyze the reduction reaction. Despite the chance of oxidation of Ti_3C_2, the oxidized and hydroxylated Ti_3C_2 would further promote the CO_2 conversion reaction and the interaction with the intermediate carbonated products. Not to mention the preference of Ti_3C_2 to chemisorb CO_2 over H_2O, which eases the reduction process by promoting H^+ and donating electrons. For the sake of comparison, the reason behind why Ti_3C_2 QDs/Cu_2O NWs/Cu exhibits an outstanding performance over Ti_3C_2 sheet/Cu_2O NWs/Cu would be owed to the positive potential of Ti3C2 sheets (0.71 V), which is undesirable for the catalyzation conversion reaction.[59]

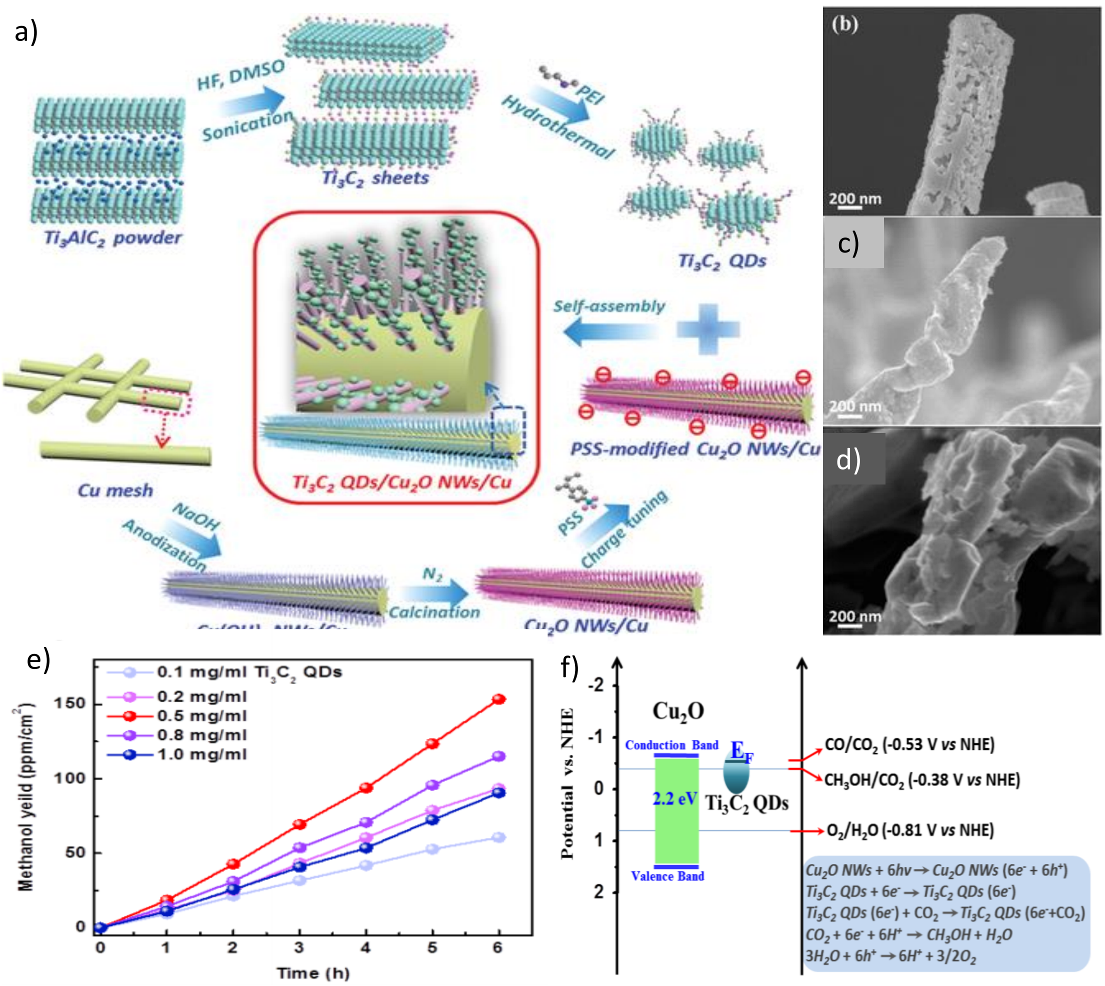

Figure 2.4: a) Fabrication scheme for Ti3C2 QDs/Cu2O NWs/Cu. Field emission scanning electron microscopy b) Cu2O NWs/Cu c) Ti3C2 QDs/Cu2O NWs/Cu d) Ti_3C_2 sheets/Cu_2O NWs/Cu. e) production rate of methanol for Ti3C2 QDs/Cu2O NWs/Cu, f) proposed reaction mechanism.[59]

Furthermore, a novel of ultrathin 3D hierarchical Co-Co layered double hydroxide/MXene nanosheet (Co-Co LDH/Ti_3C_2) nanoarrays synthesized through an in-situ MOF strategy as a co-catalyst for photocatalytic CO2 reduction.[56] 3D Co-Co LDH/MX was prepared by mixing exfoliated Ti_3C_2 of different dosages with Co^{2+} and 2-Methylimidazole (2-MIM), then the formed ZIF-67/MX nanosheets went through a solvothermal process. The proposed fabrication mechanism is as follows, the hydrolysis of $Co(NO3)_2.6H_2O$ would produce H+ that slowly etch ZIF-67 polyhedrons, releasing Co^{+2}. After that, No3- and dissolved O_2 partially oxidize the released Co+2 and then co-precipitate with Co2+ and Co+3 forming a 2D LDH structure. Hence, 2D Co-Co LDH vertical sheets incorporated electrostatically on MXene nanosheets forming a 3D hierarchical structure as shown in SEM (Fig. 2.5a). The clear boundary can be observed from TEM and HRTEM (Fig. 2.5b,c) between the Co-Co LDH and the Ti_3C_2. Furthermore, EDX mapping shows the uniformity in the element's distribution (Fig. 2.5d). The photoreduction performance for CO_2 for the prepared samples was conducted in MeCN: H_2O: TEOA (3:2:1) solution including $[Ru(bpy)_3]Cl_2.6H_2O$ as a photosensitizer.[56]

The hybrid samples show a significant enhancement over the pristine Co-Co LDH in the photocatalytic performance converting CO_2 to CO and H_2. The optimized sample Co-Co LDH/MX-15 generates the highest reported conversion rate for CO, which is 2.2 times the pure Co-Co LDH (1.25 x 10^4 µmol g-1 h -1) and 63.9% selectivity compared to the other hybrids. Such a result reflects the role that the MXene plays in the photocatalytic enhancement, which is attributed to the fast and efficient electron transfer through the interface, allowing abundant CO_2 reduction at the Co-active sites. It is noteworthy to point out that the MXene showed almost no photocatalytic activity; hence, increasing the dosage of MXene will severely decrease the conversion rate.[56] To further elucidate the catalytic enhancement for the 3D hierarchical structure for Co-Co LDH/MX-15, a 2D/2D stacked morphology (Co-Co LDH+Mx-15) was prepared by a physical mixing pure 2D Co-Co LDH with 2D MXene for the sake of comparison. The 2D/2D structure yields a 4.11 µmol h -1 and 2.44 µmol h -1 conversion rate for CO and H_2, respectively. Compared with other Co-based photocatalysts[100-108], Co-Co LDH/MX-15 showed the highest apparent quantum efficiency (AQE) of 0.92% at 420 nm. Not to mention, the Co-Co LDH/MX-15 cocatalyst maintains good stability while holding 90% of its initial conversion after five cycles. The proposed mechanism for the photoreduction process initiated by the irradiation of light on $[Ru(bpy)_3]Cl_2$ forming an excited $[Ru(bpy)_3]Cl_2^*$ then reduced to $[Ru(bpy)_3]Cl_2^-$ by TEOA. Subsequently, electrons transfer from $[Ru(bpy)_3]Cl_2^-$ to the active sites of cobalt in Co-Co LDH/MX reducing CO_2 to CO. At the same time, the protons in the solution are reduced by the excited electrons forming H_2. The Mott-Schottky plot displays a value of -1.01 V (vs. NHE) for Co-Co LDH/MX-15, which falls within the redox potential of E ($Ru(bpy)_3^{2+*}$/ $Ru(bpy)_3^+$) (-1.09 V) and E (CO_2/CO) (-0.53 V) confirming the applicability of electrons to transfer from $[Ru(bpy)_3]Cl_2$ to Co-Co LDH/MX.[56]

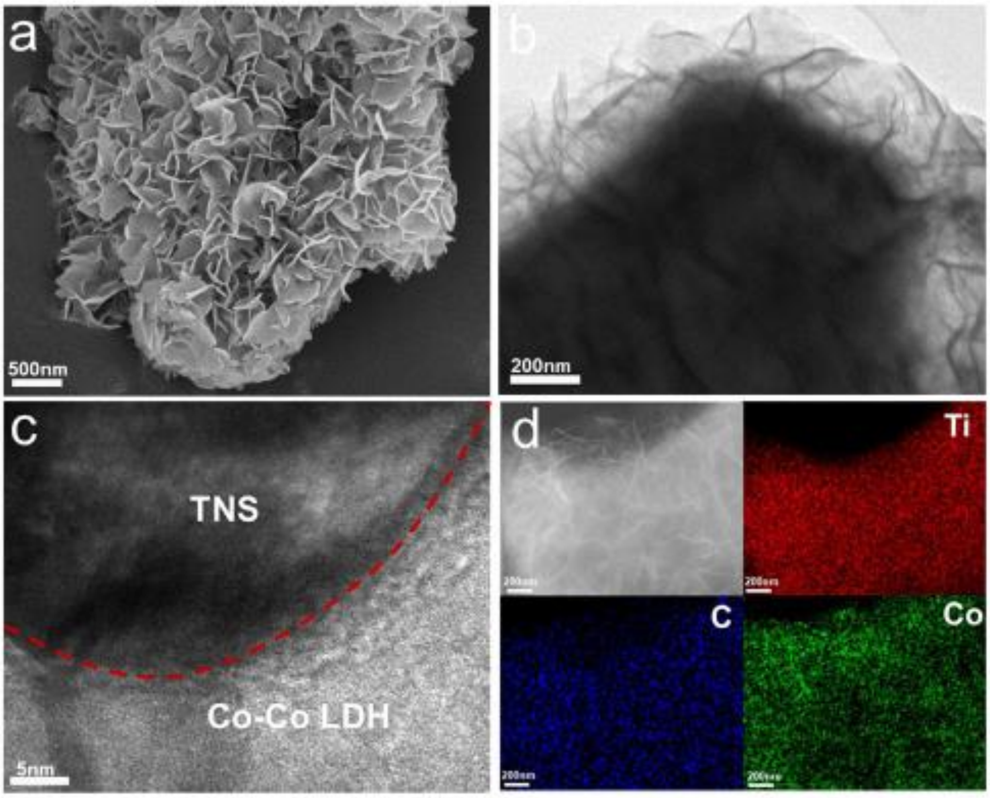

Figure 2.5: Co-Co LDH/MX-15 (a) SEM, (b) TEM, (c) HR-TEM, and (d) EDX mapping.[56]

In-situ growth of perovskite nanocrystal CsPbBr3 on two-dimensional MXene nanosheets constructing CsPbBr2/Ti_3C_2 nanocomposite was fabricated, confirming its potential application.[57] The photocatalytic reduction of CO_2 was carried out in a sealed reaction vessel, where the photocatalyst was dispersed in ethyl acetate, and the vessel was filled with CO_2 gas under solar light. The ethyl acetate selection as the solvent was based on the high solubility of CO_2 in ethyl acetate and that the $CsPbBr_3$ nanocrystal catalyst would remain stable as it has a moderate polarity. As a result of the photoreduction of CO_2, a selective linear yield for CO and CH_4 was obtained. CsPbBr3/Ti_3C_2 was found to exhibit the highest yield of CO (26.32 µmol g-1 h -1) and CH_4 (7.25 µmol g-1 h -1) in comparison to its hybrids, the pristine catalyst $CsPbBr_3$ (<4.4 µmol g-1 h -1), and other $CsPbBr_3$-based catalyst composites.[109-114]

In another approach, CeO_2/Ti_3C_2 Schottky junction was fabricated through an in-situ growth of cube-like CeO_2 and 2D ultrathin Ti_3C_2 nanosheets via hydrothermal treatment.[115] The fabrication method started by adding Cerium nitrate hexahydrate ($Ce(No_3)_3.6H_2O$) with a cube-like morphology (Fig. 2.6a) to MXene solution with an ultrathin sheet morphology (Fig. 2.6b) and left stirring for 2h then interjected in NaOH solution under vigorous stirring for 3h. Finally, the mixture went through a hydrothermal treatment at 180 C for 24 h to produce several samples of CeO_2/Ti_3C_2 with different Ti_3C_2 content. The TEM image (Fig. 2.6c) displays an intimate contact between the cube-like structure grown on the surface of Ti_3C_2 sheets of CeO_2/Ti_3C_2-5%. HRTEM (Fig. 2.6d) shows the lattice facets (002) of both CeO_2 (0.27 nm) and Ti_3C_2 (0.216 nm) corresponding to the integration of CeO_2/Ti_3C_2 hybrid with a homogenous elemental distribution of Ce, O, C, and Ti (Fig. 2.6e-i).[115] The Photocatalytic CO_2 reduction took place in a pyrex reactor containing the prepared sample, $NaHCO_3$, HCl, and 0.6 mL of CO_2 gas, under the irradiation of light.

The photocatalytic performance of the hybrid samples showed a conversion rate for CO higher than the pristine catalyst. The highest conversion rate was for CeO_2/Ti_3C_2-5% (40.2 μmol m-2 h-1), which is 1.5 that of the pure CeO_2. This result confirms that the photocatalytic performance of the catalyst was enhanced while being coupled with Ti_3C_2. The enhanced photocatalytic CO_2 reduction of CeO_2/Ti_3C_2-5% is owned by the induced build-in electric field upon the coupling of CeO_2 of the bandgap (W1=4.69 eV) with Ti_3C_2 of bandgap (W2=5.78 eV) (Fig. 2.6j). Before light illumination, the induced built-in electric field caused the electrons to transfer from the cocatalyst Ti_3C_2 to the catalyst CeO_2, bending the conduction band upwards, forming a Schottky junction with Ti_3C_2.

After illumination, the electrons are photoexcited and transferred from CeO2 crossing the Schottky barrier and reaching the surface of Ti_3C_2, promoting the photogenerated charge separation. Meanwhile, the Schottky barrier acts as a barrier to resist the recombination of the electrons to CeO_2 and repels the holes from reaching Ti_3C_2, causing the photoexcited electrons to accumulate on the surface of Ti_3C_2 to reduce CO_2 to CO.[115]Graphitic carbon nitride (g-C_3N_4) has attracted much attention recently for the photocatalytic reduction of CO_2 for its low cost, noble metal-free, and visible light response.[116-122] Despite its unfavorable separation and transfer of the photoexcited charges and low performance in adsorption and reduction of CO_2, several attempts have been made while coupling with noble metals[123], ZnO[124], SnS_2[125], ZIF-8[126], and KOH[127, 128] to overcome these drawbacks. Photocatalytic and photoelectrocatalytic (PEC) reduction of CO_2 have attracted a lot of attention converting solar energy to renewable chemical fuel.

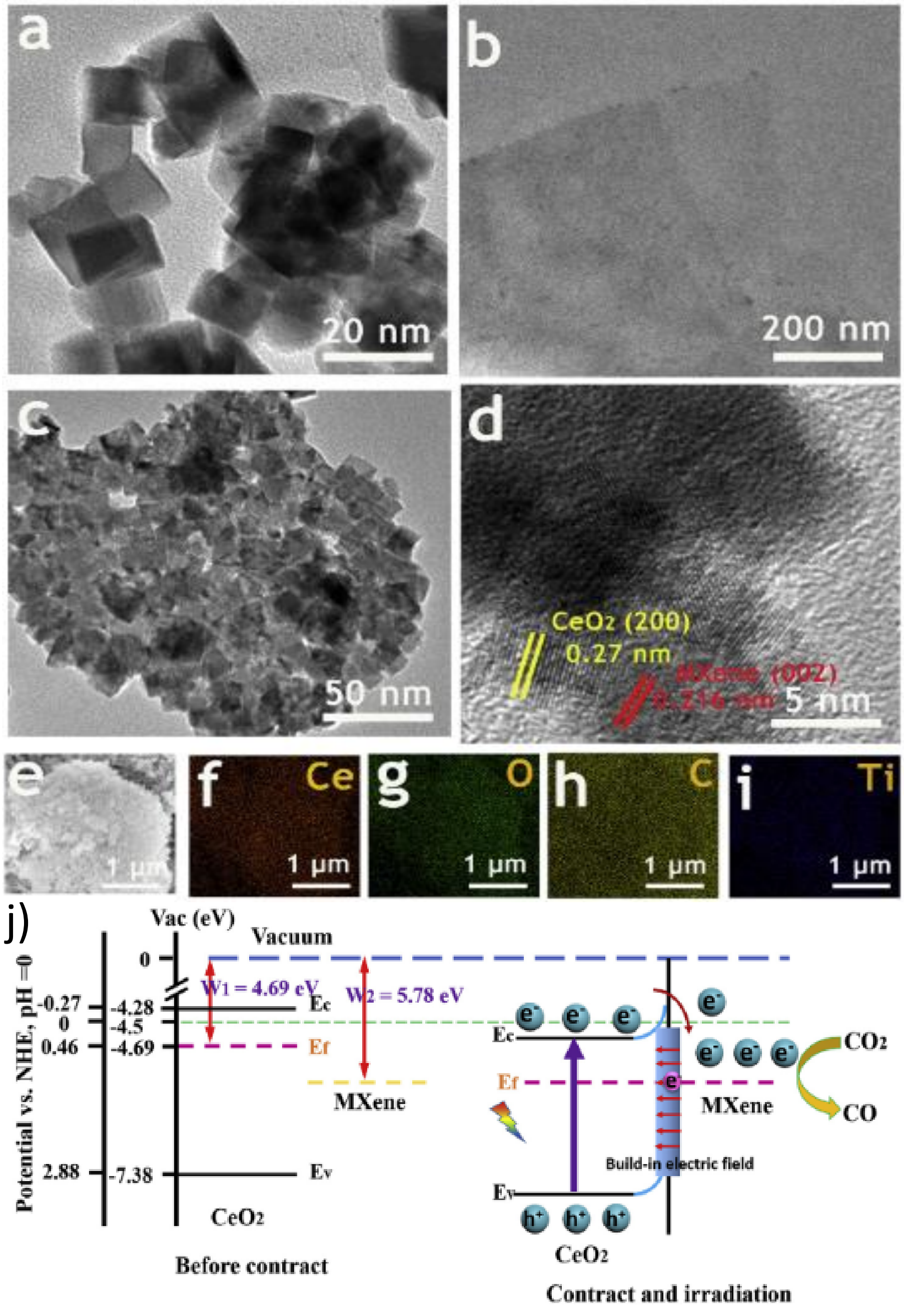

Figure 2.6: a) TEM pictures of (a) CeO_2, (b) 2D Ti_3C_2 and (c) hybrid CeO_2/MX-5%, (d) HR-TEM image and (e-i) EDX mapping of CeO_2/MX-5%. J) Electron transfer mechanism upon incoporation of Ce with Ti_3C_2.[115]

Particularly, Photoelectrocatalytic is more efficient as the externally applied voltage can fasten the charge carriers transfer while suppressing the recombination of the photogenerated electron-hole pairs. Hence, Photoelectrocatalytic reduction of CO_2

into chemical fuels in water using Ti_3C_2/g-C_3N_4 heterojunction catalyst deposited with Pd NPs synthesized by in-situ heat treatment was conducted. [129] The TEM images of the as-prepared sample display the successful incorporation of Ti_3C_2 with g-C_3N_4, as well as the NPs of Pd (Fig. 2.7a,b). The photoelectrochemical measurements were performed using a two-electrode system of Pd-g-C_3N_4 and $BiVO_4$ at -0.85 V. The catalytic performance of the photocathodes is illustrated in Fig. 2.7c, where Pd-Ti_3C_2/g-C_3N_4 exhibits the highest activity (25.1 mM h-1g-1) among the rest of the Pd-based samples. This remarkable result can be attributed to the narrow bandgap and rich Ti_3+, which are beneficial to the adsorption of solar light and the separation of electrons and holes.[129] Additionally, the considerable pyri-N species in the heterojunction has a high adsorption capability for CO_2 molecules.

Moreover, the influence of external voltage was also investigated in Fig. 2.7d. The results reveal that at a more negative voltage, the activity for hydrocarbon evolution is also increased till -0.85 V. As beyond this limit, the activity decreases because more H_2 is released. Such a result indicates that the applied voltage has an influence on the activity of the hydrocarbon evolution and the selectivity. Due to a low applied voltage, the electrons are excited from the valance band of g-C_3N_4 and Ti_3C_2 then trapped on the Pd NPs. While light irradiation, the electrons are excited by photons in the VB of g-C_3N_4 to CB. Thereafter, the photoelectrons incorporate with protons to produce active H atoms that protonate CO_2 into hydrocarbons.[129]

Most recently, due to its excellent conductivity and good susceptibility, MXene, namely surface-alkalinized Ti_3C_2, was simply mixed with g-C_3N_4 as a co-catalyst for photocatalytic reduction for CO_2.[46]

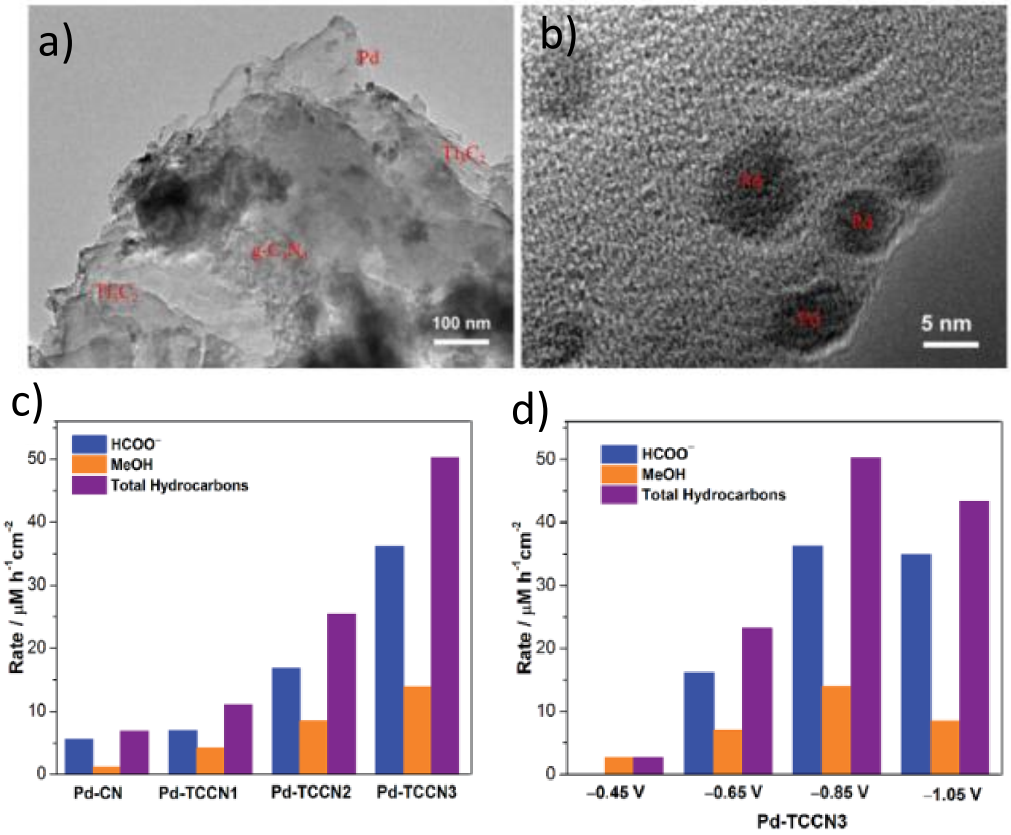

Figure 2.7: TEM images of Pd-TCCN3 at a) 100 nm and b) 5 nm. The hydrocarbon production rate for different c) MXene concentrations and d) applied voltage.[129]

TEM images elucidate the morphology and microstructure of the prepared samples, displaying a 2D nanosheets structure for the MXene after alkalization process (TCOH) (Fig. 2.8a), 2D pristine g-C_3N_4 (CN) (Fig. 2.8b). The same morphology was maintained for the resultant 5%TCOH-CN (as the 5% corresponds to the wt% of TCOH in the sample) after coupling TCOH with CN (Fig. 2.8c) along with a uniform element distribution confirming an intimate contact between TCOH and CN (Fig. 2.8d-i). The photocatalytic reduction was executed in a continuous flow system in a stainless-steel reactor maintained at constant temperature (30 °C) while applying H_2O as a hydrogen source.[46]

The photocatalytic reduction of CO_2 performance (Fig. 2.8j) displayed CO as the main product with 90% selectivity and methane (CH_4) with 10% selectivity along with a negligible trace of hydrocarbons such as C_2H_4 and CH_3CHO. All the TCOH-CN samples with different TCOH content showed a much higher conversion rate for both CO and CH_4 compared to the pristine CN (Fig. 2.8k). The highest conversion rate reported was for 5%TCOH-CN (11.21 µmol/g), which is approximately 5.9 times the production rate of pure CN. Upon increasing the TCOH loading, the conversion rate decreases as the excess TCOH prevents the catalyst CN from absorbing light. Pure MXene mixed with CN (5%TC-CN) was prepared to study the effect of the surface-modified MXene.[46] The photocatalytic performance of (5%TC-CN) resulted in 35% reduction in the CO production rate (7.23 µmol/g), yet still of a higher rate than that of pure CN (1.88 µmol/g), manifesting the efficiency of surface alkalinized MXene (TCOH) as better cocatalyst than pure MXene in the photocatalytic reduction of CO_2 when coupled with CN. Not to mention that 5%TCOH-CN almost exhibits a stable production rate for 5 cycles, indicating a stable photocatalytic activity.[46]

Moreover, Core-shell structured Ti_2O_2/C_3N_4 composite terminated by Ti_3C_2 QD on the surface of C_3N_4 (2D/2D/0D $Ti_2O_2/C_3N_4/Ti_3C_2$) were fabricated for a photoreduction of CO_2 into hydrocarbon fuels.[130] The synthesis process of $Ti_2O_2/C_3N_4/Ti_3C_2$ is as shown in Fig. 2.9a, where 2D mesoporous TiO_2 was prepared via hydrothermal-induced solvent-confined monomicelle self-assembly and then coated by C_3N_4 through thermal condensation of urea, forming 2D/2D core-shell Ti_2O_2/C_3N_4 nanosheets. Finally, Ti_3C_2 QD was prepared from a typical fabrication route followed by hydrothermal treatment and assembled on the surface of C_3N_4 via electrostatic attraction forming 2D/2D/0D $Ti_2O_2/C_3N_4/Ti_3C_2$.

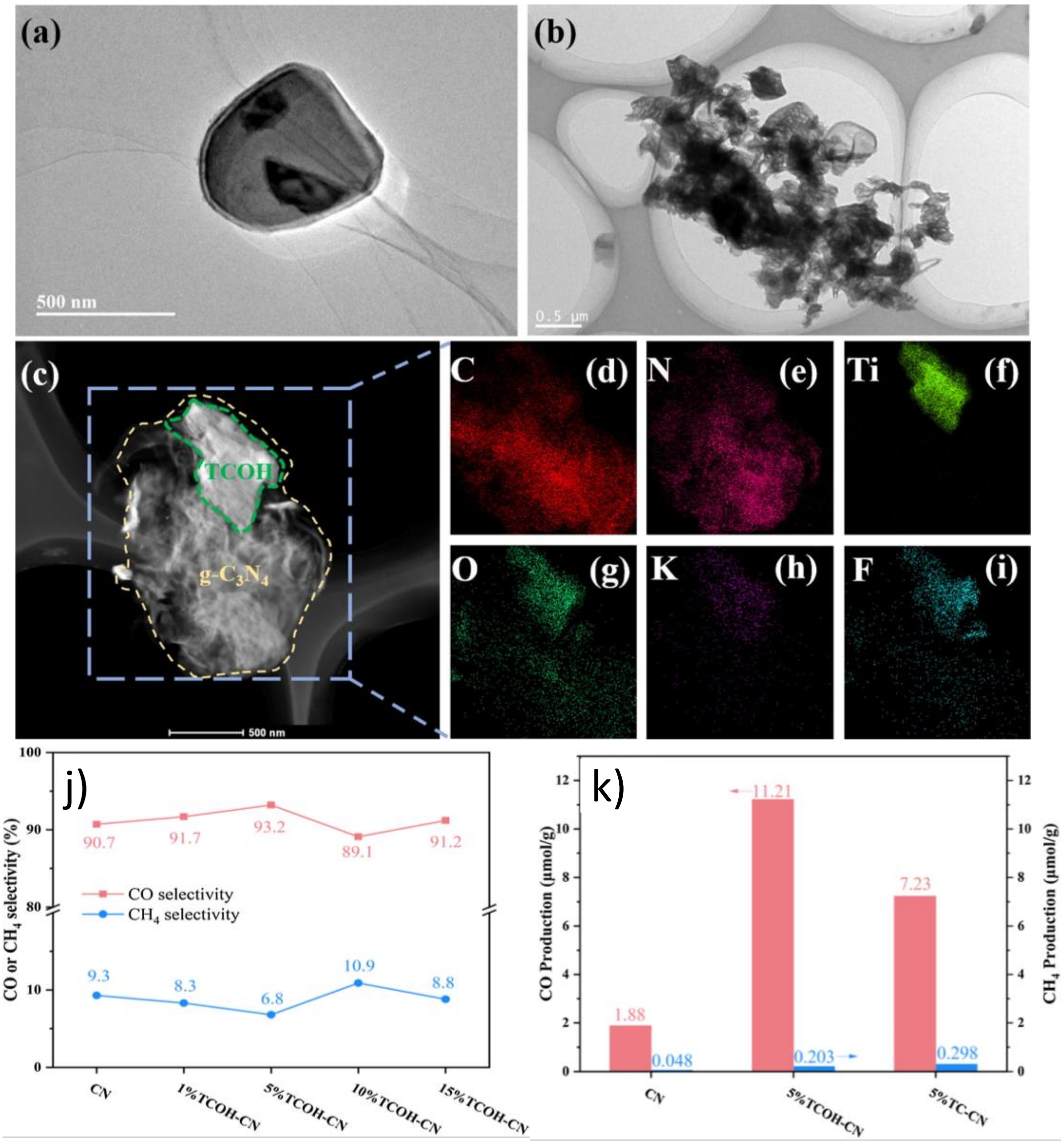

Figure 2.8: TEM picture of (a) alkalinized MXene, (b) CN. C) TEM and d-i) EDX mapping of 5% alkalinized MXene-CN. J) CO and CH_4 selectivity of CN and X%TCOH-CN, and K) Production pre-catalyst mass for the prepared samples after 5hr.[46]

The SEM analysis displays intertwined sheets for the as-prepared sample Fig. 2.9b. the TEM further confirms the entrapment of Ti_3C_2 QD in between TiO_2/C_3N_4 core-shell sheets Fig. 2.9c. The photocatalytic performance of the as-prepared samples is illustrated in Fig. 2.9d. The production rates of CO and CH_4 are minimum for the single components, and the rates were more than doubled upon their combination (Ti_2O_2/C_3N_4).[130]

It is worth noting that the thickness of C_3N_4 is adjusted by urea since a thin or thick layer of C_3N_4 results in limiting the photocatalytic reduction efficiency. As for $Ti_2O_2/C_3N_4/Ti_3C_2$, the rates of CO and CH_4 were more than three (4.39 µmol g−1−1h) and eight (1.20 µmol g−1−1h) times, respectively, than that of Ti_2O_2. The enhancement in performance is own to the accelerated spatial separation of charge carriers with a relatively strong redox feature within the heterojunction C_3N_4/Ti_3C_2 due to a low Fermi level and strong physical and electronic coupling.[130] The characteristic feature of Ti_3C_2 QD as an electron reservoir was further enhanced by C_3N_4/Ti_3C_2 than C_3N_4. Not to mention the surface groups that provide active sites and increase the surface area, increasing the gathered photoexcited electrons to facilitate multielectron reduction reaction of CO_2. The charge transfer mechanism within $Ti_2O_2/C_3N_4/Ti_3C_2$ heterojunction is represented by S-scheme. As a result of a higher Fermi level of C_3N_4 than Ti_2O and Ti_3C_2, upon contact, a spontaneous tendency for the electrons was created, migrating electrons from a high Fermi level to a lower one till equilibrium level is reached.[130] The redistribution of electrons resulted in bending the CB and VB and creating an internal electric field. Under irradiation, the electrons in Ti_2O and C3N4 were excited to their VB, and due to the internal electric field, the Ti_2O photoexcited electrons recombined with C_3N_4 holes. Whereas the C_3N_4 electrons in VB migrate to the conductive Ti_3C_2 QD driven by the potential difference. This mechanism manifests that C3N4 is the source of electrons upon irradiation and Ti_3C_2 QD acts as an electron reservoir.[130]

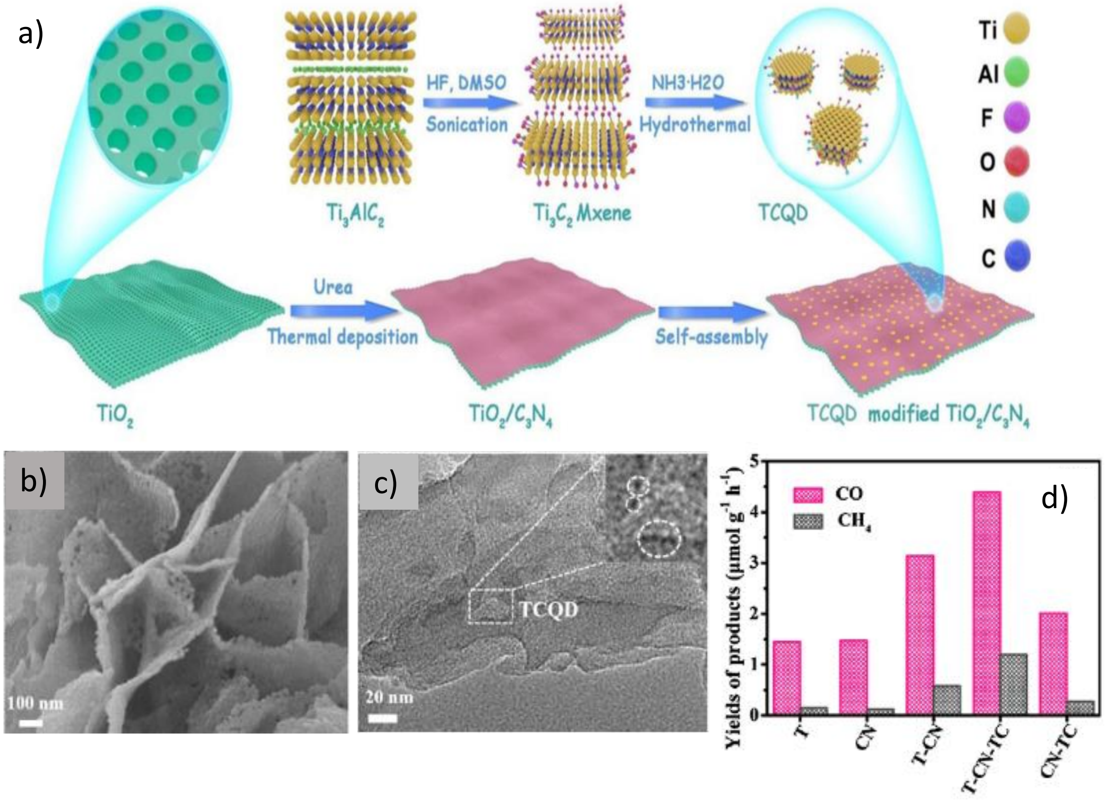

Figure 2.9: a) The fabrication scheme of TCQD anchored TiO_2/C_3N_4 core-shell nanosheets. $TiO_2/C_3N_4/Ti_3C_2$ composite b) SEM and c) TEM pictures. d) production rate of the prepared samples after 1h.[130]

An ultrathin 2D/2D Ti_3C_2/g-C_3N_4 heterojunction was fabricated by calcination for Ti_3C_2 and urea for CO_2 photocatalytic reduction.[48] Briefly, as shown in Fig. 2.10, Ti_3C_2 was etched typically and dispersed in a urea solution with high concentration then sonicated, allowing the urea to intercalate into the interlayers of Ti_3C_2 sheets. The mixture was then dried and calcinated at high temperatures, where the urea is polymerized and simultaneously acts as a source of the NH_3 gas template to exfoliate Ti_3C_2 and produce g-C_3N_4 crafted on the surface of Ti_3C_2. This facile preparation method is much less costly and time-consuming, as it nether involves the usage of hazardous DMSO for a long time intercalation nor repeated washing. Finally, it can greatly improve the production yield of Ti_3C_2 than the conventional preparation method. The obtained heterostructure exhibits superior photocatalytic performance in reducing CO_2 to CO and CH_4. The optimal sample (10TC) exhibits the highest conversion rate for CO (5.19 μmol g−1h−1) and CH_4 (0.044 μmol g−1−1h), outperforming previously reported g-C_3N_4 based catalysts. whereas both Ti_3C_2 and g-C_3N_4 displayed a weak photocatalytic performance due to the metallic behavior and the fast recombination of the photoexcited electron-hole pairs, respectively.

Moreover, the photocatalytic performance remained almost constant after five consecutive cycles. Such a remarkable performance can be attributed to the intimate contact between g-C_3N_4 and Ti_3C_2 that integrates the migration and separation of photoexcited charge carriers. The proposed mechanism for the heterojunction composite entails that upon incorporation, the Fermi level for each of Ti_3C_2 and g-C_3N_4 comes to equilibrium at -0.95 V, allowing the photoexcited electrons to migrate first from the VB to CB of g-C_3N_4. Subsequently, migrate to the surface of Ti_3C_2 owned to the intimate contact interface between the two materials. Hence, the accumulated electrons on the Ti_3C_2 surface participate in the CO_2 reduction reaction.[48]

Ti_2CT_x and Mo_2CT_x were investigated in electrocatalytic CO_2 reduction reaction owning to Ti and Mo metals weak hydrogen binding behavior.[131] The process was performed in a two-compartment electrochemical cell (Fig. 2.11a) using a mixture of 80:18:5 mol fraction of acetonitrile: water: $BMIMBF_4$ as an electrolyte. The selection of the electrolyte was based on the dominant HER in the aqueous electrolyte ($KHCO_3$). The solubility of CO_2 is enhanced using acetonitrile compared to the aqueous electrolyte, likely by forming complexes with CO_2 at (-0.1 V VS SHE).

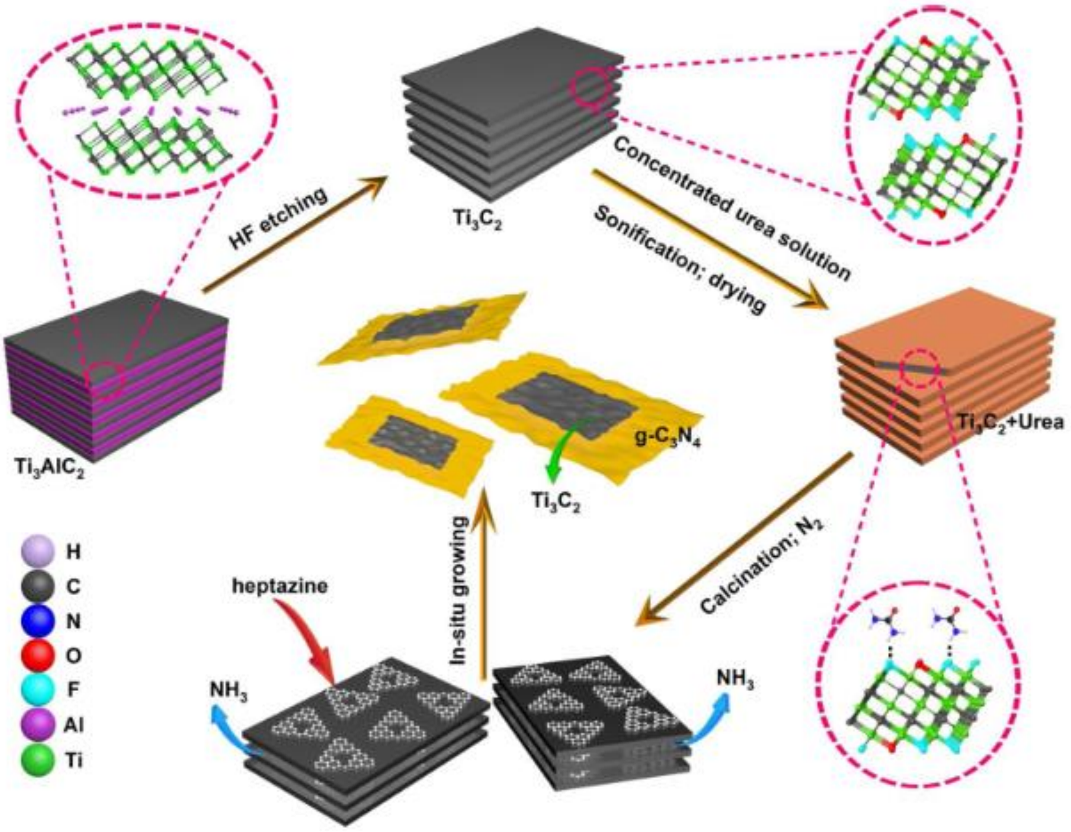

Figure 2.10: Synthesis process of 2D/2D Ti_3C_2/g-C_3N_4 nanosheets heterojunction.[48]

Through subjecting the samples to chronoamperometric measurement, online GC and NMR analysis indicated that formic acid and H_2 were the major products for Ti_2CT_x at onset potential (-1.5 V). whereas Mo_2CT_x converts CO_2 to formic acid a lower potential (-0.9 V). The Faradaic efficiency plot (Fig. 2.11b) displays 56.1% and 20.7% for formic acid at -1.8 V of Ti_2CT_x (KF-HCL) and Ti_2CT_x (HF), respectively.[131] Noting that Ti_2CT_x (HF) has much –F surface terminations than Ti2CTx (KF-HCl). Although Faradaic efficiency of Mo_2CT_x is 32.6% for formic at -1.3 V, its partial current density (Fig. 2.11c) is significantly higher than -2.5 mA.cm^{-2} indicating higher activity to convert CO2 to formic acid compared to Ti_2CT_x.

Furthermore, DFT calculations were completed to investigate the influence of varying the percentage of terminal groups between F and O on the overpotential of the CO_2 reduction process.[131] The proposed mechanism follows two hydrogenation steps to obtain and desorb formic acid, following the *COOH pathway. The energy diagram of Ti_2CT_x (Fig. 2.11d) clearly illustrates that the first hydrogenation step is the limiting step, more importantly, the variation of the energy barrier of the limiting step upon varying the percentage of the terminal group. Fully terminated O on Ti2CTx surface has the lowest energy barrier (0.85 eV) and as the O content decreases, the energy barrier increases. On the other hand, the potential limiting step for CO_2 reduction on Mo_2CT_x is affected by the amount of the terminal group (Fig. 2.11e). At fully O terminated Mo_2CT_x, the second hydrogenation step was the limiting step (0.47 eV), and as the F content increased by 11% or more, the energy barrier of the first hydrogenation step increases and becomes the limiting step.[131]

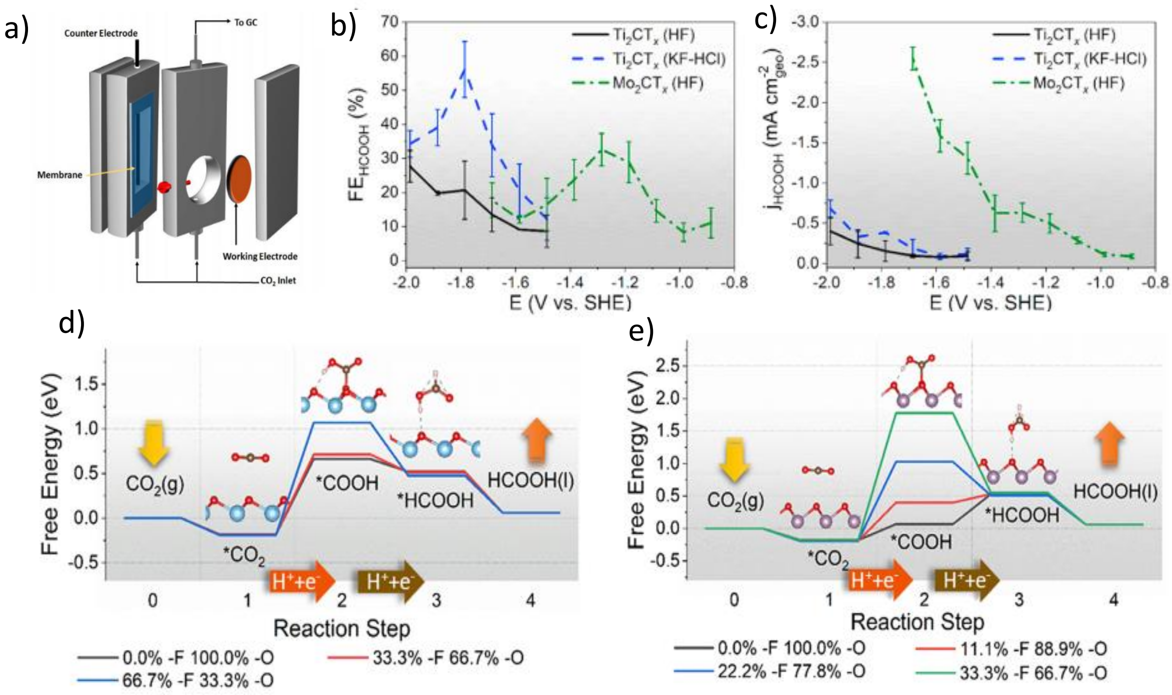

Figure 2.11: a) The used electrochemical cell. b) Faradaic efficiency and c) current density on Ti_2CT_x and Mo_2CT_x MXenes. The proposed path way for (d) Ti_2CT_x and (e) Mo_2CT_x at different functional groups such as –F and –O.[131]

Further studies were reported on MXenes theoretically with screening several phases such as; 2D MXenes of group (IV, V, and VI) with formula M_3C_2 have been hypothesized to function as a catalyst for electrochemical reduction of CO_2 to energy-rich hydrocarbon products on the basis of metal-terminated surfaces and metallic character that MXenes exhibit.[41] From a mechanism perspective, the conversion process of CO_2 undergoes series of electrochemical reductions by a set of pair of H+/e-. Based on the total even number (up to eight) of H+/e- pair participating in the reaction, different hydrocarbons can be produced. Hence, the electrochemical mechanism of CO_2 reduction using transition metal carbides (M_3C_2) was proposed using the state-of-the-art DFT calculation with dispersion correction. The process of adsorption occurs through spontaneous chemisorption, in which CO_2 forms a bond with the active terminal transition metal leading to its capture. The calculated Gibbs free energy using PBE/DFT-D2 and the state-of-the-art PBE/DFT-D3 illustrates that group IV-VI M_3C_2 exhibits a spontaneous capability -with group IV being the strongest- to capture CO_2.[41]

Nevertheless, group VI (Cr_3C_2 and Mo_3C_2) showed a less negative value of Gibbs free energy for chemisorption of H_2O over CO_2. Explicitly, the proposed system overcomes major limitations encountered previously, such as the fixation of CO_2 at high temperature and pressure to enhance the capture of CO_2 and the competitive reduction reaction of H_2O and CO_2. The conversion mechanism for CO_2 using MXenes follows a path of eight successive hydrogenation steps on C and O (Fig. 2.12). Starting with spontaneous reduction forming OCHO, followed by OCH_2O, $HOCH_2O$, H_2CO with the release of one H_2O molecule, and CH_3O as the fifth step. Due to the reactivity behavior of MXenes, the sixth H+/e- pair leads to the formation and release of CH_4 while O is attached to the MXene. Finally, the last two hydrogenation steps leading to the formation of OH, then a captured H_2O. Noting that the desorption of water can be either removed by relatively small energy or displaced thermodynamically by CO_2. Out of the eight different MXenes studied, Cr_3C_2 and Mo_3C_2 are the most selective candidates toward the formation of CH_4 with a 1.05 and 1.31 eV input energy, respectively.[41]

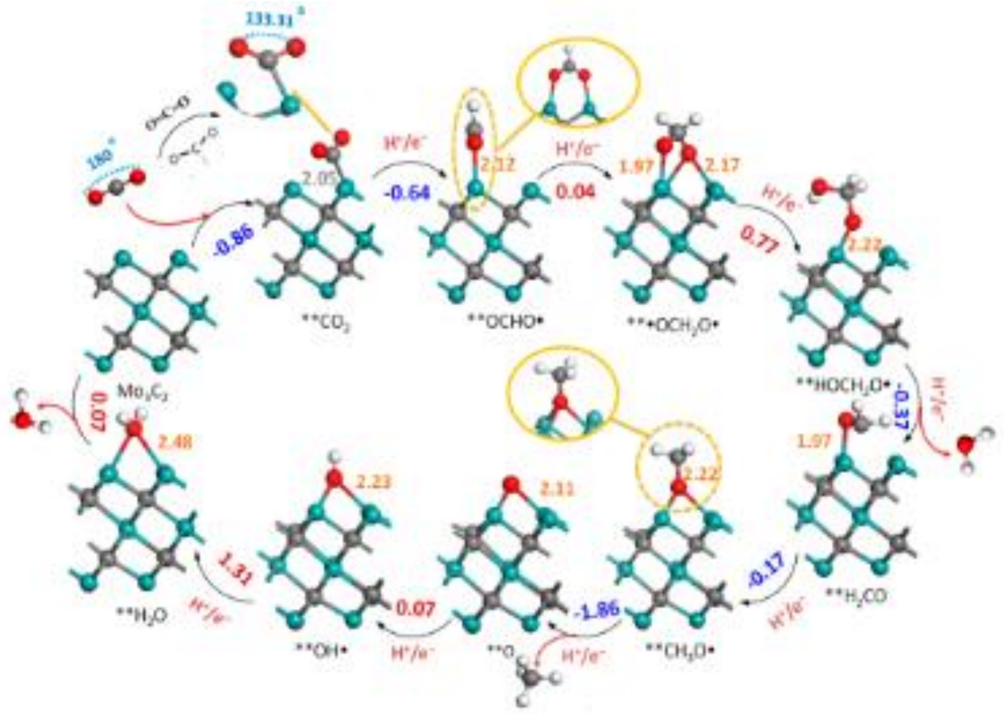

Figure 2.12: Reaction pathway for converting CO_2 into $*CH_4$ by Mo_3C_2.[41]

First-principles simulations were utilized on 17 different MXene terminated by a hydroxyl group $M_2X(OH)_2$ in exploring the catalytic effect and mechanism of CO_2 reduction into CH_4.[40] In an aqueous solution, bare MXenes are unstable and usually terminated by either oxygen or hydroxyl group or a mixture of both. According to the experimental results, the hydroxyl group is stable and energetically favored for most investigated MXenes, especially at a negative potential. The CO_2 conversion process into CH_4 follows a multistep transfer of 8 H+/e- pair (Fig. 2.13a).

The proposed alternative reaction pathway with the lowest energy was achieved by forming more stable intermediates by capturing a hydrogen atom from the surface termination OH group by some of the intermediates. It was found that some of the intermediates tend to temporarily capture the H form -OH group donated as (H) and eventually returned it to the catalyst as the reaction progresses.

On the other hand, specific intermediates (steps 4 and 5) tend to permanently capture and hold on to the H atom donated as [H].[40] As a result, a hydrogen vacancy is created (slab-nH) on the surface of the MXene. And with a little energy, the vacancy is recovered by a donated H from the H+/e- pair to the catalyst in the final step. The theoretical calculations reveal that MXenes that have the tendency for a high hydroxyl coverage, such as $Sc_2C(OH)_2$ and $Y_2C(OH)_2$ are the most promising for the CO_2 reduction reaction with a limiting potential of -0.53 and -0.61 V, respectively.

The utilization of the simultaneous capture of H atom from the OH group and the solution enables the transformation of CO_2 and CO into *(H)COOH and *(H)CHO in a single step with low activation energy. Eliminating the requirement of intermediates such as *COH, *CHO, and *COOH are considered to be a limiting potential for CO_2 reduction reaction on transition metal surface. It is worth noting that the bond between H and O in the OH terminal group plays its role in selecting the potential limiting step for $M_2X(OH)_2$. A very weak bonding would refer to *(H)COOH to *CO as the limiting step since returning the temporarily captured (H) would be difficult. However, if the bonding is very strong, CO_2 to *(H)COOH would be considered as the limiting step as it requires capturing H from the terminal group[40] Hence, the ideal case to achieve the most favorable overall limiting potential is when the two previously mentioned steps have the same limiting potential. As for the studied $M_2X(OH)_2$ specifically, *(H)COOH to *CO is the limiting step for most of them with

$Sc_2C(OH)_2$ and $Y_2C(OH)_2$ at the peak of the volcano curve (Fig. 2.13b), referring to a relatively strong O-H bonding and the least overall limiting potential making these two candidates the most promising catalysts among the studied $M_2X(OH)_2$.[40]

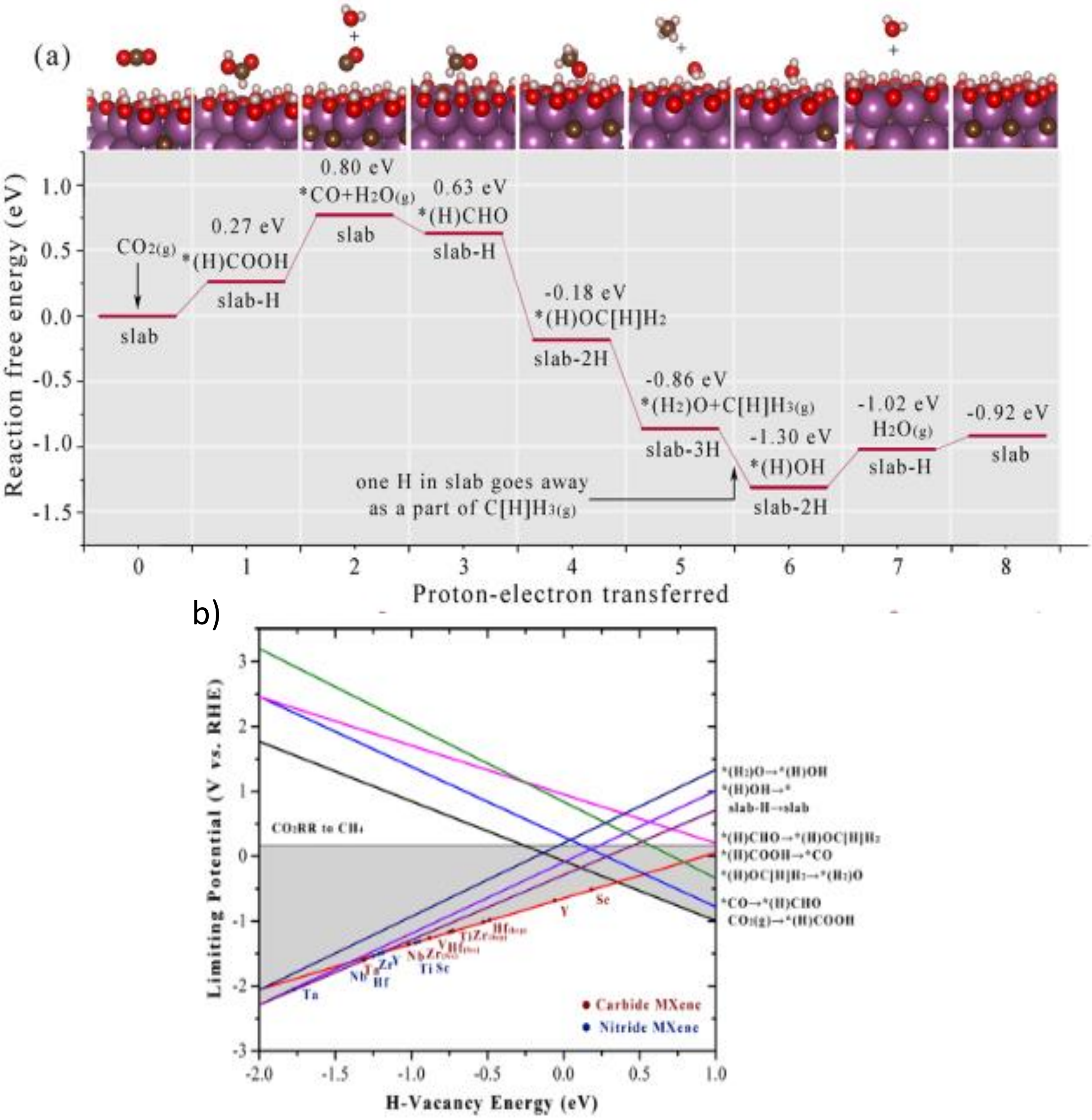

Figure 2.13: a) reaction pathway on -OH terminated Mxene $Sc_2C(OH)_2$ to convert CO_2 to CH_4. b) Volcano curve of OH-terminated MXenes.[40]

Additionally, O-terminated monolayer MXene TiCO2 with oxygen vacancy has been identified using DFT as the most promising catalyst for photocatalytic CO_2 reduction between $Ti_3C_2O_2$ and V_2CO_2[132]. Despite the high tendency for CO_2 adsorption, Ti_2CO_2 also has a high selectivity for formic acid (HCOOH). The proposed reaction pathway (Fig. 2.14) follows the adsorption of CO2 at the oxygen vacancy for Ti_2CO_2 (-0.73 eV), then hydrogenated twice to form HCOOH by overcoming the 0.53 eV barrier, which is much lower than the formation step of CH_4, CH_3OH, and HCHO. Further hydrogenation was found to be less favorable than the desorption of HCOOH.[132] The catalytic reduction of CO_2 can be attributed to the oxygen vacancy on $TiCO_2$. Hence introducing more oxygen vacancies on O-terminated MXene can further enhance the reduction of CO_2 to hydrocarbons. Abundant of oxygen vacancy can be generated on full O-terminated MXene by CO and H2 based on the following reaction: CO + H2 + MXene (perfect) →HCOOH+ MXene (Ov), as the adsorption of CO_2 on the O-terminated MXene with oxygen vacancy equals to that of CO on full O-terminated MXene.[132]

DFT calculations were utilized to explore the electroreduction of CO_2 to CH_4 on 19 O-terminated MXene phase “M_2XO_2”, where M: Sc, Ti, Zr, Hf, V, Nb, Ta, Cr, Mo, and W; and X: C and N.[133] Based on Pourbaix diagram analysis, most of the studied MXene monolayers are full of O group corresponding to the lowest free energy, except for Sc MXene. The electroreduction process is based on 8 H+/e- pair transfer for the hydrogenation of CO_2. The proposed pathway (Fig. 2.15a,b) follows an alternating binding between -H and -C coordination for the intermediates on the O-terminated MXene surface, achieving the lowest energy for the formation of CH_4.[133] It is noteworthy to point out that out of the 19 studied M_2XO_2 phases, the lowest energy path was the same except for V_2CO_2, Ta_2CO_2, and Cr_2CO_2. Both W_2CO_2 and Ti_2CO_2 were the most promising for the CO_2 reduction reaction with a limiting potential of -0.35 V and -0.52 V, respectively. Besides, it was found that the binding energy of C-bounded intermediates is highly correlated. Similarly, the H-bounded intermediates indicating a linear scale of bounding energy with respect to *COOH and *HCOOH, respectively(Fig. 2.15c-e).[133]

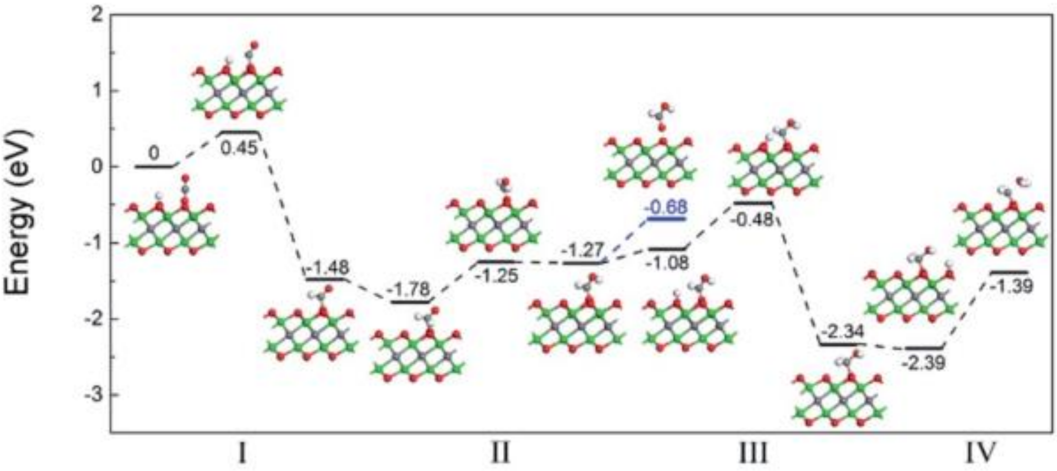

Figure 2.14: Hydrogenation mechanism of CO_2 on the surface of oxygen defective Ti_2CO_2.[132]

Finally, the first principle calculations were used to study the properties of 9 phases of MXenes "M_2C" for efficient adsorption and reduction of CO_2.[134] The adsorption Gibbs free energy plot illustrates (Fig. 2.16a) spontaneous and exothermic adsorption of all the investigated phases owned to negative free energy. As shown in the figure's inset, the C-O bond has been elongated and the angle has been decreased upon adsorption on the surface of Mo_2C, indicating CO_2 activation. Additionally, the adsorption of H_2O was less negative than the adsorption of CO_2, indicating a higher selectivity for CO_2 capture.[134] After identifying the more energetically preferred intermediate (OCHO*) and the most favorable route for the CO_2 reduction process, all the energy paths for all the proposed M_2C phases were calculated.

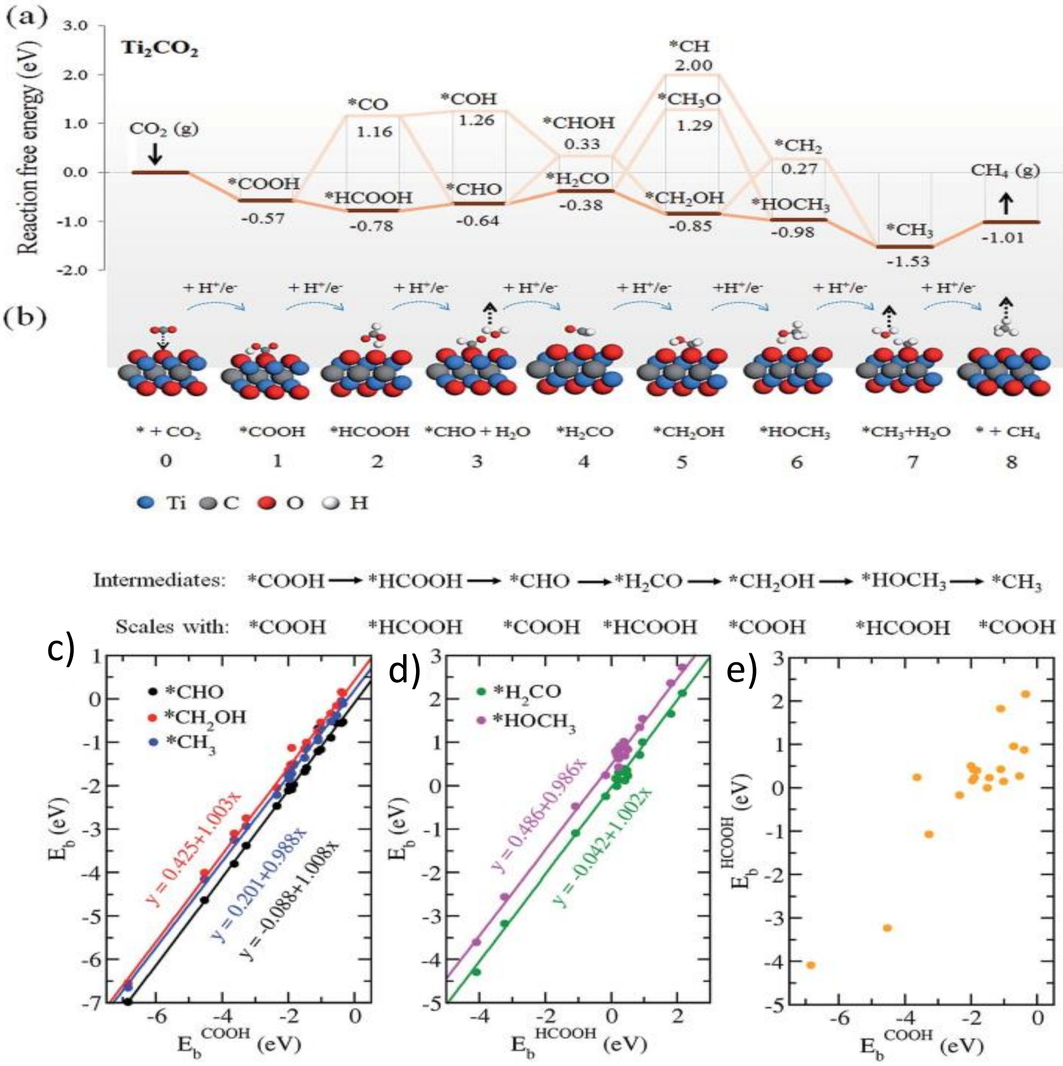

Figure 2.15: a) Free energy diagram and (b) ball-and-stick model illustrating several pathways to produce CH_4 on Ti_2CO_2. c-e)Adsorption energies of CO_2 reduction reaction on M_2XO_2 for different intermediates.[133]

Upon comparing the first hydrogenation step, group VI MXenes (Cr_2C, Mo_2C, and W_2C) with negative free energy were the best candidates (Fig. 2.16b). To further narrow the competition, the 8th hydrogenation step, which acts as the limiting step for all the candidates owned to its high energy barrier, was the smallest for Mo_2C (1.19 eV). Noting that a higher barrier was reported experimentally on (100) surface bulk

Mo_2C (1.49 eV). This result nominates Mo_2C as a promising catalyst for CO_2 reduction reaction experimentally, especially that Mo_2C with a free surface group has been obtained experimentally.[135]

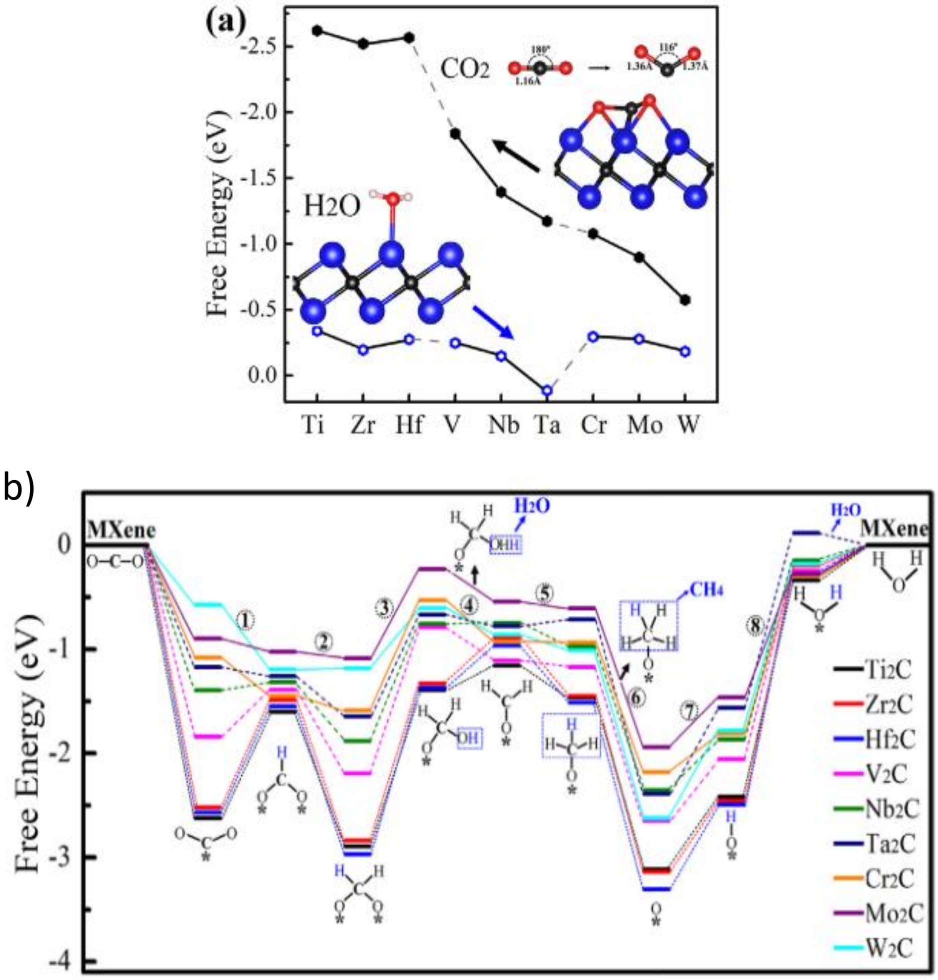

Figure 2.16: a) Gibbs free energies of CO_2 and H_2O on different phases of M_2C MXenes. b) Pathway for CH_4 production for several M_2C phases. [134]

Conclusion:

In summary, this overview reports MXene as a recently discovered material and its role as a catalyst and cocatalyst in the electrocatalytic and photocatalytic reduction of CO_2 from both experimental and theoretical perspectives. MXene, as an economical and efficient material, demonstrated in the experimental work an outstanding enhancement for the photocatalytic performance of CO_2 reduction. This is mainly due to the increased active surface area and enhanced charge transfer, carrier density, light absorption, and stability, despite the negligible photocatalytic performance of MXene alone without the main catalyst.

CHAPTER 3: MATERIALS AND METHODOLOGY

3.1 CHEMICALS AND MATERIALS

Titanium aluminum carbide (Ti_3AlC_2) purchased from Carbon-Ukraine Ltd. Dimethyl sulfoxide (C_2H_6OS) purchased from Fisher Scientific International. Hydrofluoric acid (HF) bought from VWR Chemicals BDH. Acetone (CH_3COCH_3, ≥ 99.9 %), Potassium tetrachloropalladate (II) (Cl_4K_2Pd) (98%), Copper (II) nitrate trihydrate (($Cu (NO_3)_2.3H_2O$, 99%), and Cobalt (II) chloride (97%) were purchased from Sigma-Aldrich Chemie GmbH (Munich, Germany).

3.2 METHODOLOGY

3.2.1 Synthesis of $Ti_3C_2T_x$ nanosheets

Two-dimensional $Ti_3C_2T_x$ nanosheets were fabricated by selective chemical etching. Where 1 g of Ti_3AlC_2 powders were added slowly to an HF aqueous solution (10 ml, 48 Wt. %) while stirring at room temperature for 24h, then washed at 4500 rpm with deionized water until the pH ≥ 5.5-6. Thereafter, the etched MAX sediment was further washed with ethanol once, and the remaining wet powder was left in the oven for overnight to dry. The dry powder was then dispersed in DMSO (15 mL) under magnetic stirring for 24 hours at room temperature. The resultant solution was centrifuged at 4500 rpm to remove the unreacted DMSO, and then the remaining sediment was dispersed in water and sonicated for 5 hours while purging nitrogen. The final delaminated Ti_3C_2Tx product was isolated by centrifugation at 4000 rpm for 1 h to isolate the desired product.

3.2.2 Synthesis of Pd-M/$Ti_3C_2T_x$ nanosheets

A solution of Cl_4K_2Pd (0.1 mg) and $Cu(NO_3)_2.3H_2O$ (0.1 mg) were dropwise into 25 mL of the as-prepared $Ti_3C_2T_x$ under the magnetic string at room temperature and kept under agitated stirring for 8 h. Thereafter, 50 mL of acetone was added to the solution in order to precipitate Pd-Cu/$Ti_3C_2T_x$ and kept for 2 h, then centrifuged, and the supernatant decanted, while the sediment was vacuum dried at 60^{o}C overnight. Similarly, Pd-Co/$Ti_3C_2T_x$ was prepared.

The synthesis of Pd/$Ti_3C_2T_x$, Cu/$Ti_3C_2T_x$, and Co/$Ti_3C_2T_x$ was also the same except that Potassium tetrachloropalladate (II) (98%) (0.1 mg), Cu $(NO_3)_2.3H_2O$ (0.1 mg), and Cobalt (II) chloride (97%) (0.1 mg) are added separately on delaminated $Ti_3C_2T_x$, in line with previously reported article.[136]

3.3.3 Materials characterization

The Scanning electron microscope ((SEM), Hitachi S-4800, Hitachi, Tokyo, Japan) and transmission electron microscope (TEM, TecnaiG220, FEI, Hillsboro, OR, USA) equipped with an energy-dispersive spectrometer (EDS), were used for investigation shape and composition. The X-ray photoelectron spectroscopy (XPS) spectra were recorded on a Kratos Axis (Ultra DLD XPS Kratos, Manchester, UK) along with a monochromatic Al Kα radiation source (1486.6 eV) under a UHV medium. The X-ray diffraction (XRD) was analyzed on an X-ray diffractometer (X'Pert-Pro MPD, PANalytical Co., Almelo, Netherlands) using a Cu Kα X-ray source (λ = 1.540598 Å).

3.3.4 Electrochemical CO_2 reduction reaction

Electrochemical measurements:

The electrochemical CO_2 reduction tests were carried out on Gamry potentiostat (reference 3000, Gamry Co., USA) in an H-shape cell using a three-electrode system involving a Pt wire, leak-free Ag/AgCl (KCl, 3 M)), and glassy carbon (GC) as counter centrode, reference electrode, working electrode, respectively. The catalyst ink was prepared by mixing 2 mg of each catalyst with Nafion solution (30 µL, 0.05 Wt %) in 1 mL of deionized H_2O/ethanol (3/1 v ratio) under sonication until getting a homogeneous solution. That was directly and deposited over the polished GCE electrodes and then left to dry under vacuum at 50 ^{o}C. Thereafter, the gas is purged in the electrolyte, and the electrochemical measurements are carried out such as Cyclic Voltammograms (CVs), Linear Sweep Voltammogram (LSVs), Chronoamperometry (CA), and Impedance spectroscopy (EIS).

Photoelectrochemical:

The photoelectrochemical experiment will be performed using a Gamry electrochemical analyzer (reference 3000, Gamry Co., USA). The cyclic Voltammograms (CVs) are remeasured again under UV light.

CHAPTER 4: RESULTS AND DISCUSSION

The fabrication process of Pd-M/$Ti_3C_2T_x$ begins with selectively removing the Al from Ti_3AlC_2 using HF, then intercalated with DMSO and finally exfoliated under ultrasonication to produce $Ti_3C_2T_x$ nanosheets. During the etching process of Al, the HF also etched off some of the adjacent Ti atoms owned to the high concentration of HF.[136] The 2D $Ti_3C_2T_x$ encompasses three Ti sublayers connected to carbon atom via octahedral sites, and the adjacent 2 layers are connected with Al atom. Hence, resulting in Ti vacancies and T_x surface termination functionalities such as (O_2^-, OH^-, and F^-) on Ti sublayers. Thereby, after doping Pd with Cu or Co precursors with $Ti_3C_2T_x$, both Pd-Cu and Pd-Co are evenly distributed atomically and homogenously inserted inside the lattice structure of $Ti_3C_2T_x$, owned to the ability of the surface termination group and the Ti-vacancies that can reduce Pd-Cu and Pd-Co precursors electrostatically, easing the accommodating of Pd-Cu and Pd-Co in the unstable and reductive Ti vacancies forming Pd-Cu/$Ti_3C_2T_x$ and Pd-Co/$Ti_3C_2T_x$.

The SEM image of bulk Ti_3AlC_2 illustrated its typical stacked and dense 3D structure (Fig. 4.1a). After removing the Al atom and exfoliation process, the 3D MAX phase is transformed to 2D $Ti_3C_2T_x$ multilayered sheets with terminal groups (Fig. 4.1b). The size of the formed sheets ranged from 0.2 µm to 1 µm, and the sheets are highly exfoliated with an interlayer distance of 50 nm (Fig. 4.1c). Mixing Pd-Cu and Pd-Co precursor with $Ti_3C_2T_x$ further enhanced the exfoliation of the sheets owning to the doping effect. The $Ti_3C_2T_x$ sheets are thinner, and the interlayer spacing increased significantly in the case of binary doping Pd-Cu/$Ti_3C_2T_x$ (Fig. 4.1d) and Pd-Co/ $Ti_3C_2T_x$ (Fig. 4.1e). The SEM image of mono dopped Pd/$Ti_3C_2T_x$ (Fig. 4.1f), Cu/$Ti_3C_2T_x$ (Fig. 4.1g), and Co/$Ti_3C_2T_x$ (Fig. 4.1h) also displayed multilayered delaminated sheets structure with deformed edges.

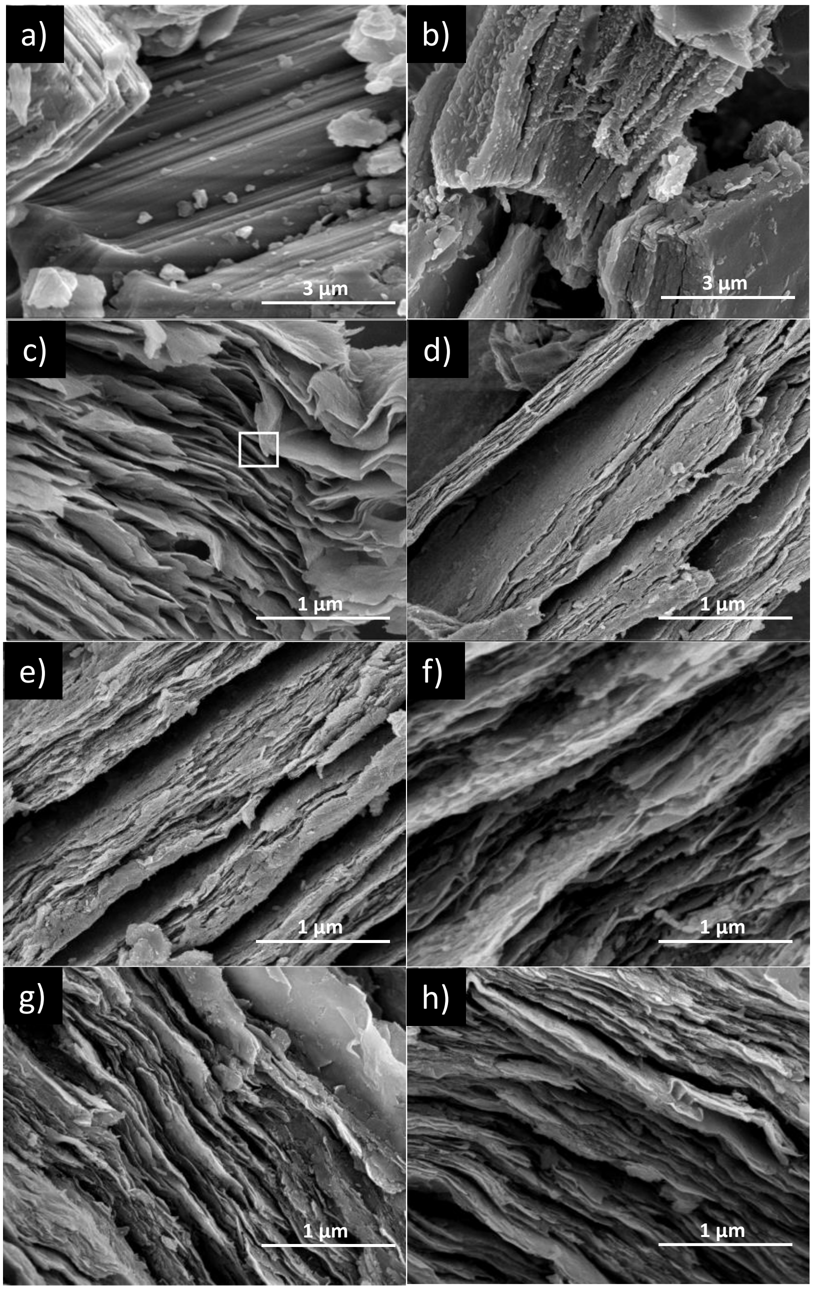

Figure 4.1: SEM images for a) MAX phase, b,c) $Ti_3C_2T_x$, d) Pd-Cu/$Ti_3C_2T_x$, e) Pd-Co/$Ti_3C_2T_x$, f) Pd/$Ti_3C_2T_x$, g) Cu/$Ti_3C_2T_x$, and h) Co/$Ti_3C_2T_x$

The bulk compositions of the binary dopped samples Pd-Cu/$Ti_3C_2T_x$ and Pd-Co/$Ti_3C_2T_x$ compared to $Ti_3C_2T_x$ were studied using the element mapping and EDX. The element mapping for binary doped samples demonstrates the co-existence of the dopped metals along with Ti, C, and O (Fig. 4.2 & Fig. 4.3).

Furthermore, EDX confirms the existence of the doped metals as shown in (Fig. 4.4) as additional peaks appeared for the doped metals, which was not found in the EDX result of the pure $Ti_3C_2T_x$ (Fig. 4.4a). It is worth noting that the EDX for the binary doped samples Pd-Cu/$Ti_3C_2T_x$ and Pd-Co/$Ti_3C_2T_x$ (Fig. 4.4b,c) displayed higher metal content than the mono doped samples (Fig. 4.4d-f). The estimated atomic content of Pd-Cu, Pd-Co, Pd, Cu, and Co are about 1.5, 1.4, 0.65, 0.65, and 0.7, respectively, further indicating the full insertion of the metals inside the Ti_3C_2Tx lattice. Furthermore, the O content indicates the abundance of surface terminations in the as-prepared samples. This result is owned to the HF etching process and intercalation as well as the electrophilic property of the Ti, which can directly bind to O and OH groups, thereupon proving unique physiochemical merits.

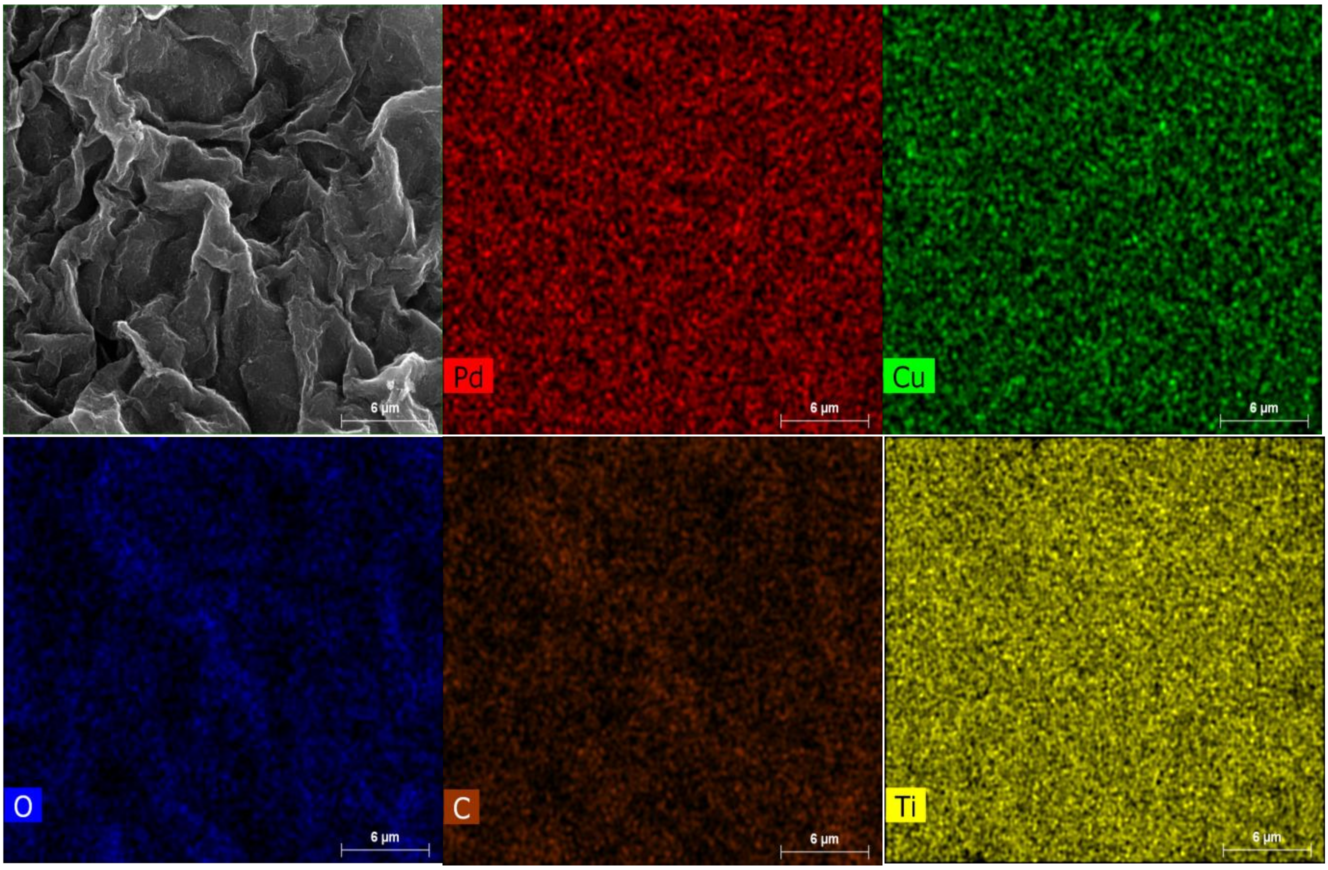

Figure 4.2: Element mapping for Pd-Cu/$Ti_3C_2T_x$

The TEM image of pristine MXene $Ti_3C_2T_x$ displayed a typical 2D structure. Whereas the TEM images for Pd-Cu/$Ti_3C_2T_x$, Pd-Co/$Ti_3C_2T_x$, Pd/$Ti_3C_2T_x$, Cu/$Ti_3C_2T_x$, and Co/$Ti_3C_2T_x$ display 2D nanosheets with wrinkled edges (Fig. 4.5 b-f), in line with the SEM images. This is also revealed the absence of Pd, Cu, and Co in the obtained samples Pd-Cu/$Ti_3C_2T_x$, Pd-Co/$Ti_3C_2T_x$, Pd-Co/$Ti_3C_2T_x$, Cu/$Ti_3C_2T_x$, and Co/$Ti_3C_2T_x$.

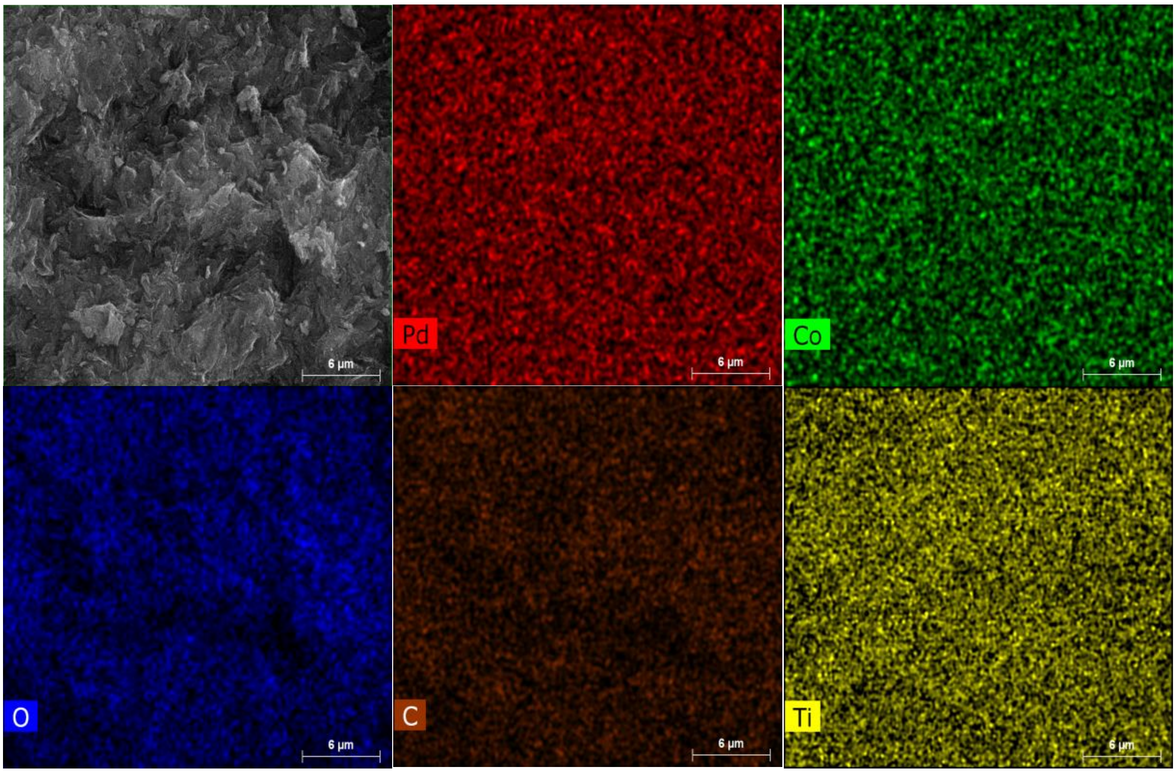

Figure 4.3: Element mapping for Pd-Co/$Ti_3C_2T_x$

Fig. 4.6 displays the XRD analysis of Ti_3C_2Tx with (002), (004), and (006) facets.[137] Similarly, metal-doped Pd-Cu/$Ti_3C_2T_x$, Pd-Co/$Ti_3C_2T_x$, Pd/$Ti_3C_2T_x$, Cu/$Ti_3C_2T_x$, and Co/$Ti_3C_2T_x$ displayed the same facets confirming the successful doping (Fig. 4.7). Such a result further confirms the absence of any diffraction peaks for Pd, Cu, and Co metals or their oxides in agreement with previous reports[136, 138], owning to their low content. Moreover, no facets were found for TiO_2 nanoparticles, indicating that the as-prepared $Ti_3C_2T_x$ MXene is uniform.[136, 138]

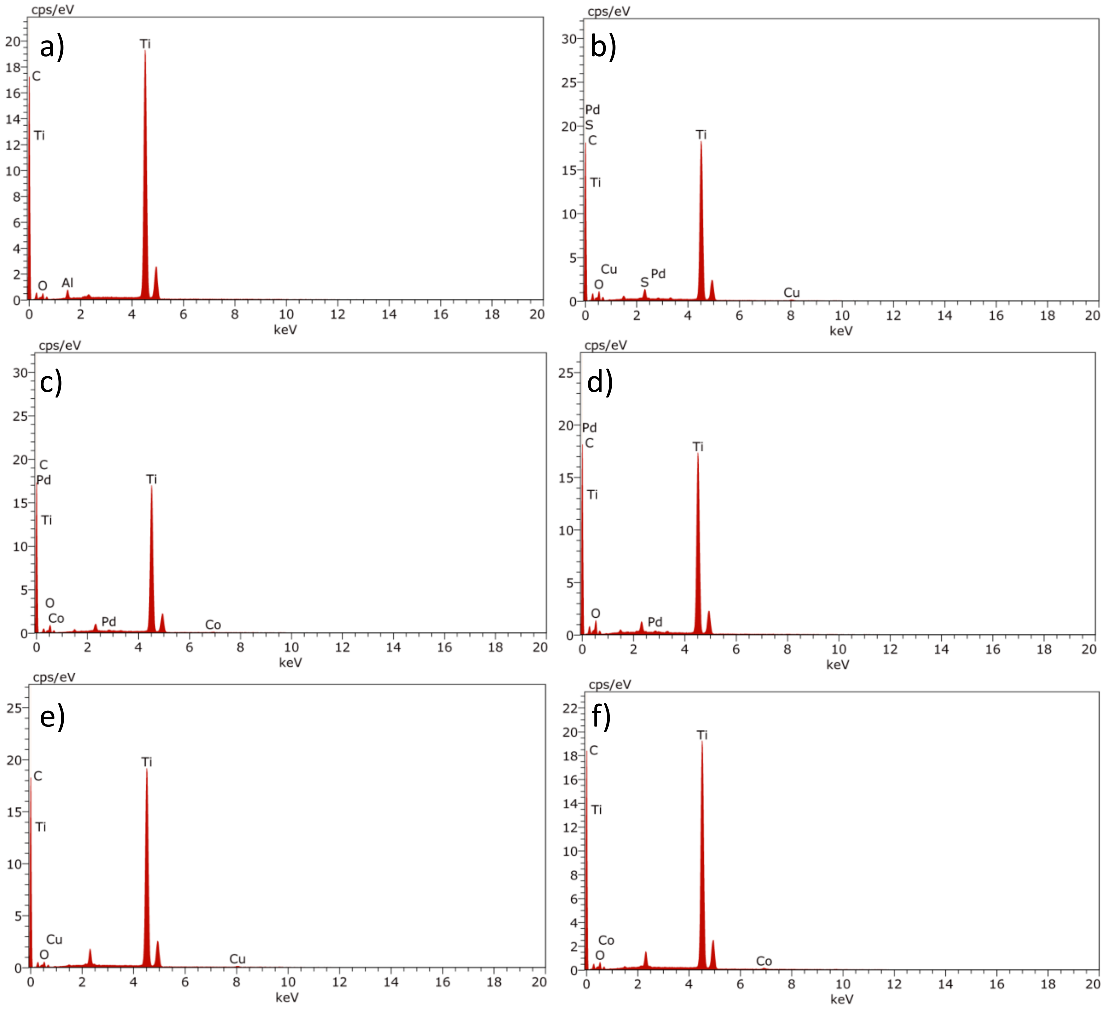

Figure 4.4: EDX analysis for a)Ti3C2Tx, b)Pd-Cu/$Ti_3C_2T_x$, c)Pd-Co/$Ti_3C_2T_x$ d)Pd/$Ti_3C_2T_x$, e)Cu/$Ti_3C_2T_x$, and f)Co/$Ti_3C_2T_x$.

The XPS analysis was used to get more insights on the surface composition, chemical and electronic state states of thus formed materials. Fig. 4.8a reveals the XPS surveys for Pd-Cu/$Ti_3C_2T_x$, Pd-Co/$Ti_3C_2T_x$, Pd/$Ti_3C_2T_x$, Cu/$Ti_3C_2T_x$, and Co/$Ti_3C_2T_x$ compared to pristine $Ti_3C_2T_x$, which all display the valence band of Ti 2p, C 1s, O 1s, and F 1s. Meanwhile, Pd 3d and Cu 2p spectra were detected in Pd-Cu/$Ti_3C_2T_x$, Pd/$Ti_3C_2T_x$, and Cu/$Ti_3C_2T_x$.

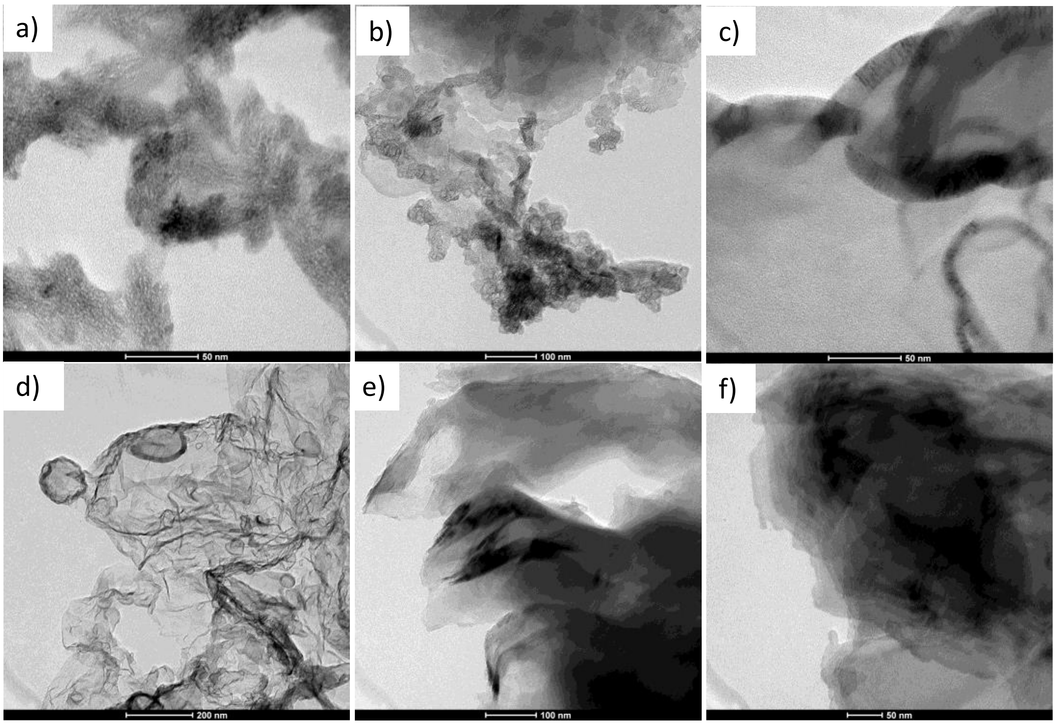

Figure 4.5: TEM images for a)$Ti_3C_2T_x$ b)Pd-Cu/$Ti_3C_2T_x$ c)Pd-Co/$Ti_3C_2T_x$ d)Pd/$Ti_3C_2T_x$ e)Cu/$Ti_3C_2T_x$ f)Co/$Ti_3C_2T_x$.

In the high-resolution XPS spectra Fig. 4.8b for Pd-Cu/$Ti_3C_2T_x$ sample, Pd 3d is deconvoluted into 2 peaks, Pd 3d5/2 and Pd 3d3/2 at 336.5 eV and 341.75 eV assigned to Pd metal. Similarly, Cu 2p (Fig. 4.8c) is deconvoluted into 2 metal peaks Cu 2p3/2 (933 eV) and Cu 2p1/2 (952.2 eV). As for Pd 3d and Co 2p in Pd-Co/$Ti_3C_2T_x$, the Pd 3d spectra showed the same peaks as the Pd 3d in Pd-Cu/$Ti_3C_2T_x$, whereas the Co 2p spectra displayed Co 2p3/2 at 779.2 eV and Co 2p1/2 at 794.2 eV. The existence of the doped metals Pd, Cu, and Co further confirms the successful fabrication of doped Pd/M-$Ti_3C_2T_x$. Furthermore, the presence of both Pd-Cu and Pd-Co in the metallic state arising from their atomic doping inside the lattice of $Ti_3C_2T_x$ enriched with abundant Ti vacancies, which are highly energetic.

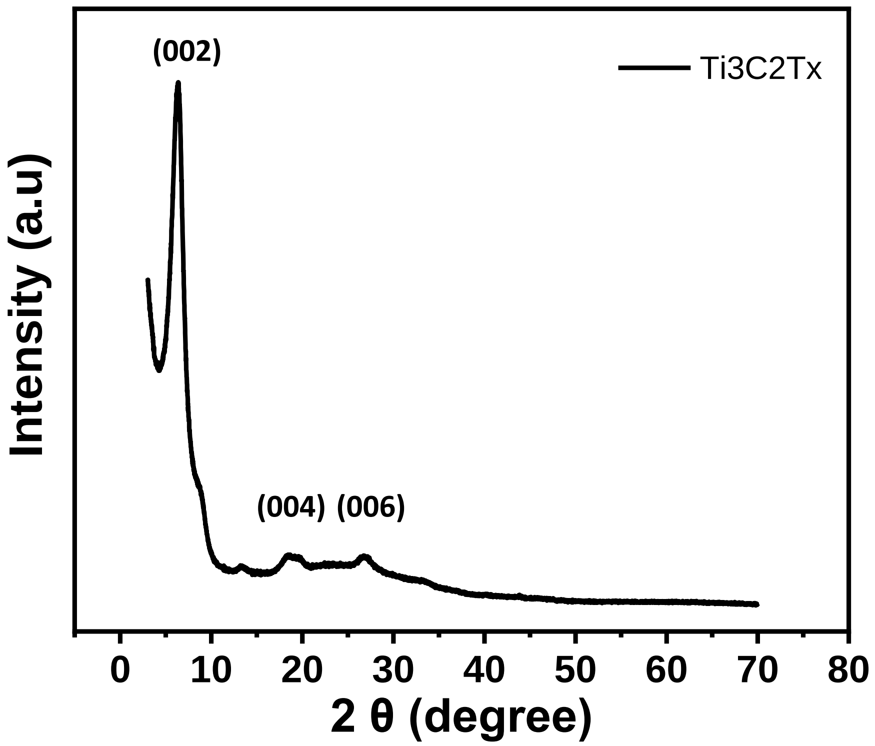

Figure 4.6: XRD pattern for $Ti_3C_2T_x$

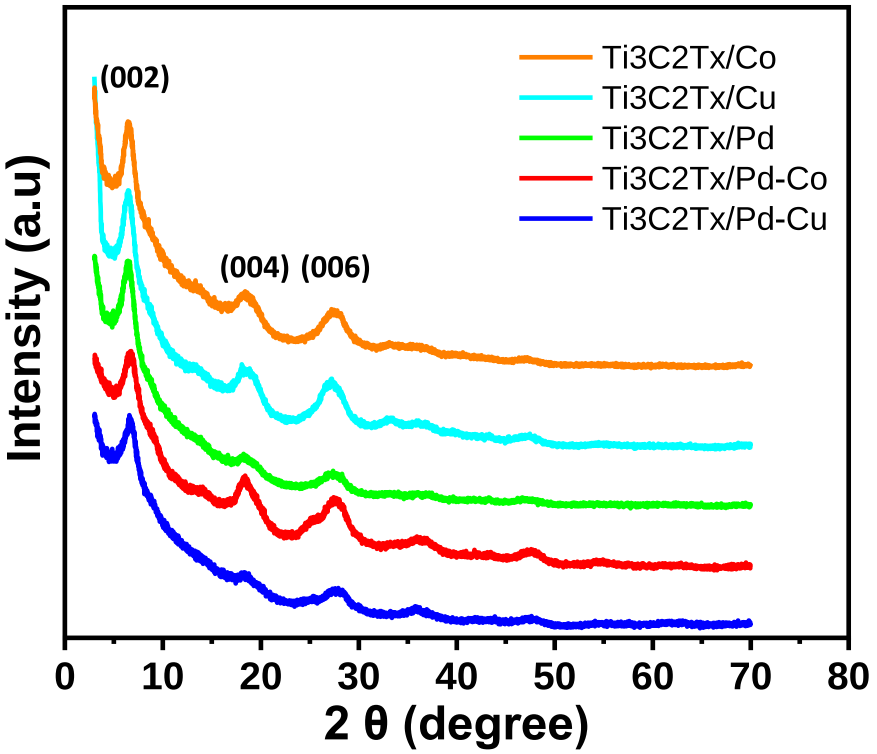

Figure 4.7: XRD pattern for the dopped samples

Fitting of Ti 2p spectra in Pd-Cu/Ti_3C_2Tx (Fig. 4.8f) were deconvoluted into four peaks, displaying 2p3/2 (455.3 eV) and 2p1/2 (461.5 eV) assigned to Ti-C. Along with, TiO 2p3/2 (459 eV) and 2p1/2 (464.8 eV). The noticed the higher intensity of Ti-C compared to TiO peaks indicates that the majority of Ti in the metallic phase form in the interior of the $Ti_3C_2T_x$. Meanwhile, the high intensity of TiO peak is attributed to chemical states of Ti atoms that are surrounded by the oxygen ions in the $Ti_3C_2T_x$ lattice, resulting from the replacement of some C atoms by O_2 during the HF etching. Deconvolution of C 1s spectra in spectra displayed C-Ti, C-C, C-O, and COOH at 281.1, 28.4, 286.4, and 289.7 eV, respectively, in thus prepared in Pd-Cu/Ti_3C_2Tx (Fig. 4.8 g). Likewise, fitting O 1s spectra display, O bonded to Ti (530 eV) and Ti (531.9 eV), indicating the abundance of O group (Fig. 4.8h). Fitting F 1S spectra displayed Ti-F at 684.6 eV and C-F at 686.8 eV.

Recently, 2D $Ti_3C_2T_x$ nanosheets have attracted much great attention for CO_2RR; however, previous reports on the theoretical performance rather than the excremental application. Unlike the literature, herein the rational design of $Ti_3C_2T_x$ doped with binary and monometallic dopants at the atomic level and emphasized the CO_2RR performance as a function of doping.

Electrochemical CO_2 reduction:

Inspired by the unique structural and compositional merits of 2D Pd-Cu/$Ti_3C_2T_x$ and Pd-Co/$Ti_3C_2T_x$ nanosheets, its CO_2RR was benchmarked compared to Pd/$Ti_3C_2T_x$, Cu/$Ti_3C_2T_x$, Co/$Ti_3C_2T_x$, and metal-free $Ti_3C_2T_x$. Prior to the measurements, 20 segments of cyclic voltammogram (CVs) were conducted between -1 V and 0.35 V at 200 mV s^{-1} in 0.1 M $NaHCO_3$ under N_2, for activation and removal of any impurities (Fig. 4.9a).

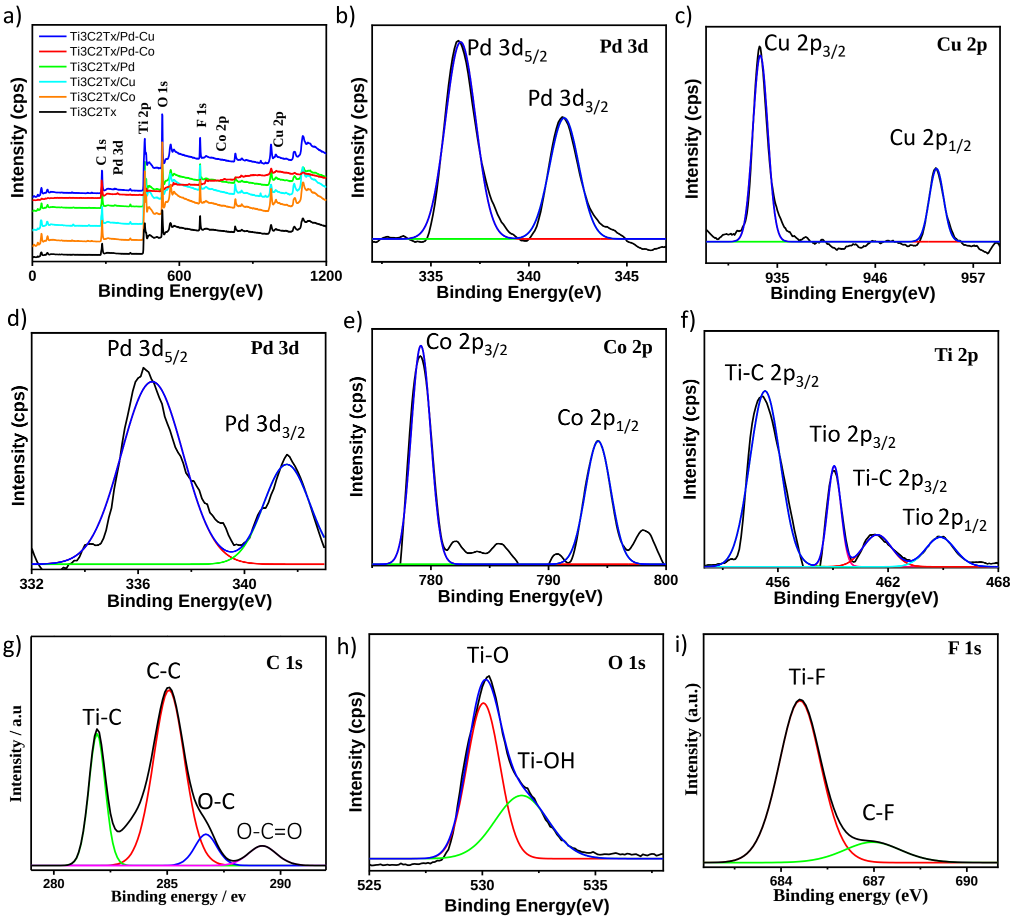

Figure 4.8: (a) XPS survey of all the prepared samples. High-resolution XPS spectra of (b,c) Pd, Cu in Pd-Cu/Ti_3C_2Tx, (d,e) Pd, Co in Pd-Co/Ti_3C_2Tx, and (f,g,h,i) Ti in Pd-Cu/Ti_3C_2Tx

Then, CVs were measured at 50 mV s^{-1} for all catalysts, which all demonstrated voltammogram features of quasi-rectangular shape indicates due to their pseudo-capacitance effect. Pd-Cu/$Ti_3C_2T_x$ nanosheets showed the highest capacitance current and hydrogen under-potential adsorption/desorption (H-UPD) at -1V than that of Pd-Co/$Ti_3C_2T_x$, Pd/$Ti_3C_2T_x$, Cu/$Ti_3C_2T_x$, Co/$Ti_3C_2T_x$, and metal-free $Ti_3C_2T_x$, due to the great interlayer spacing and accessible sites active sites of Pd-Cu/$Ti_3C_2T_x$. Also, The CVs displayed the absence of any redox peaks for Pd or Cu or Co, or Ti, and their oxides implied their stability without any oxidation or leaching during the electrochemical reaction.

The CVs curves measured 0.1 M $NaHCO_3$ under CO_2 atmospheric on the as-synthesized catalysts displayed CO_2RR voltammograms with an obvious cathodic reduction current in the negative direction potential similar to the typical cathodic reduction processes (Fig. 4.9 b). There are no resolved redox peaks for Pd, Cu, and Co implied their atomic distribution inside $Ti_3C_2T_x$. Also, Pd-Cu/$Ti_3C_2T_x$ showed a higher CO_2RR current than Pd-Co/$Ti_3C_2T_x$, Pd/$Ti_3C_2T_x$, Cu/$Ti_3C_2T_x$, and $Ti_3C_2T_x$, respectively.

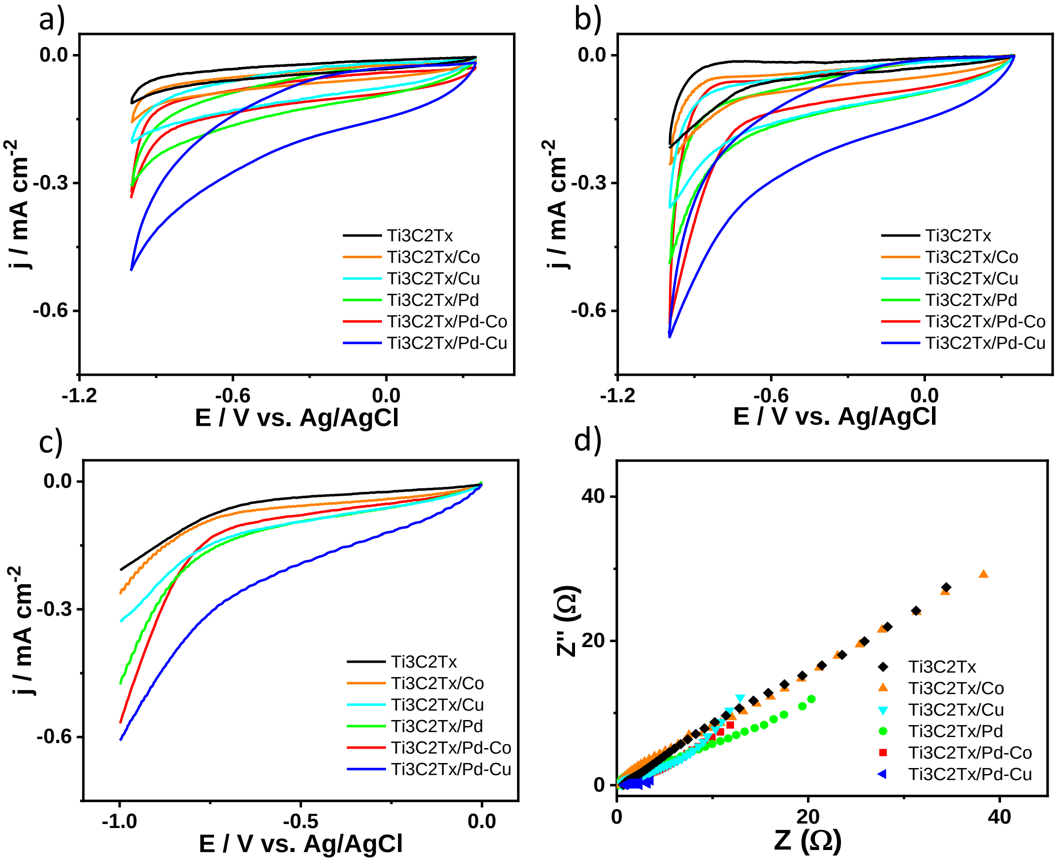

Figure 4.9: electrochemical measurements of the prepared samples a) Cv under N_2 b) Cv under CO_2 c) LSV, and d) EIS

The LSV curves reordered under CO_2 atmospheric revealed the CO_2RR cathodic current density (I_{CO_2RR}) of -0.66, -0.63, -0.39, -0.27, -0.2, and -0.18 mA cm^{-2} on Pd-Cu/$Ti_3C_2T_x$, Pd-Co/$Ti_3C_2T_x$, Pd/$Ti_3C_2T_x$, Co/$Ti_3C_2T_x$, and $Ti_3C_2T_x$, respectively (Fig.

4.9 c). This indicates the substantial effect of co-doping with Pd and Cu for enhancement of the CO_2RR current by 3.66 times than that of metal-free $Ti_3C_2T_x$. The onset potential (E_{CO_2RR}) on Pd-Cu/$Ti_3C_2T_x$ (-0.17 V) was significantly shifted to a more positive potential, infers the promote CO_2RR kinetics on Pd-Cu/Ti3C2Tx. This is furthered evidenced in the greater I_{CO_2RR} on Pd-Cu/$Ti_3C_2T_x$ that consume less poetical to produce higher I_{CO_2RR} under any potential than that on the rest of the doped samples and by extension, the metal-free sample.

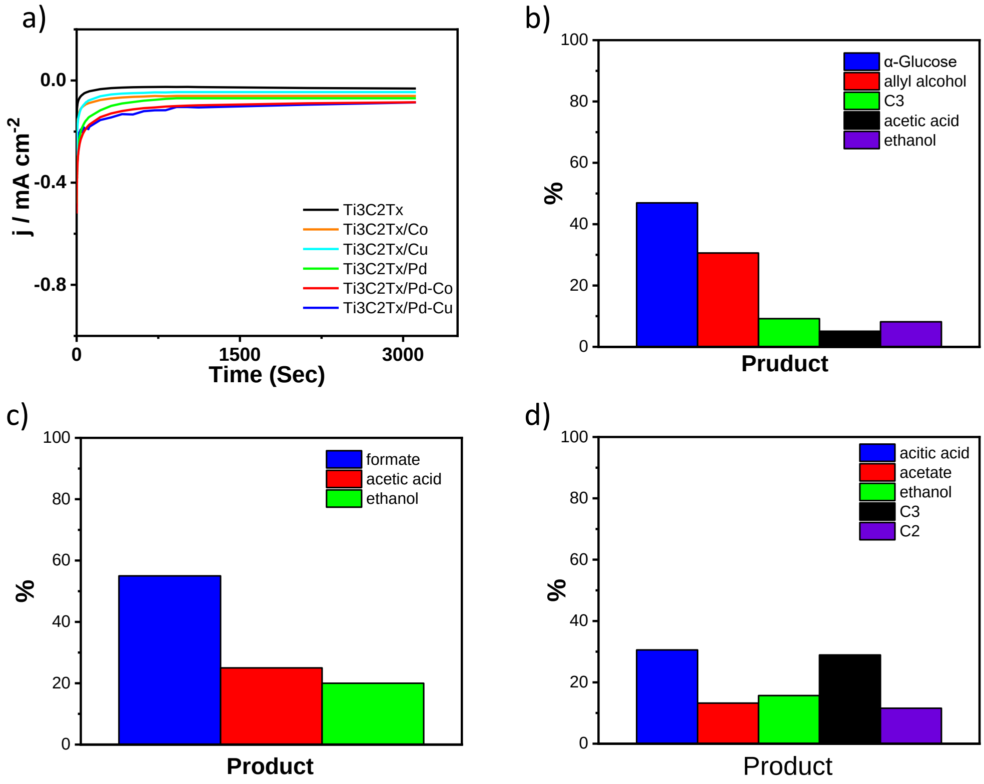

Figure 4.10: a) IT plot. Produced hydrocarbon products of b) Pd-Cu/$Ti_3C_2T_x$ c) Pd-Co/$Ti_3C_2T_x$ d) Pd-Cu/$Ti_3C_2T_x$.

To get more insights into the CO_2RR performance of the formed electrolytes, the electrochemical impedance spectra (EIS) test was tested (Fig. 4.9d). The EIS Nyquist plots of tested electrocatalysts revealed the semicircle shape.

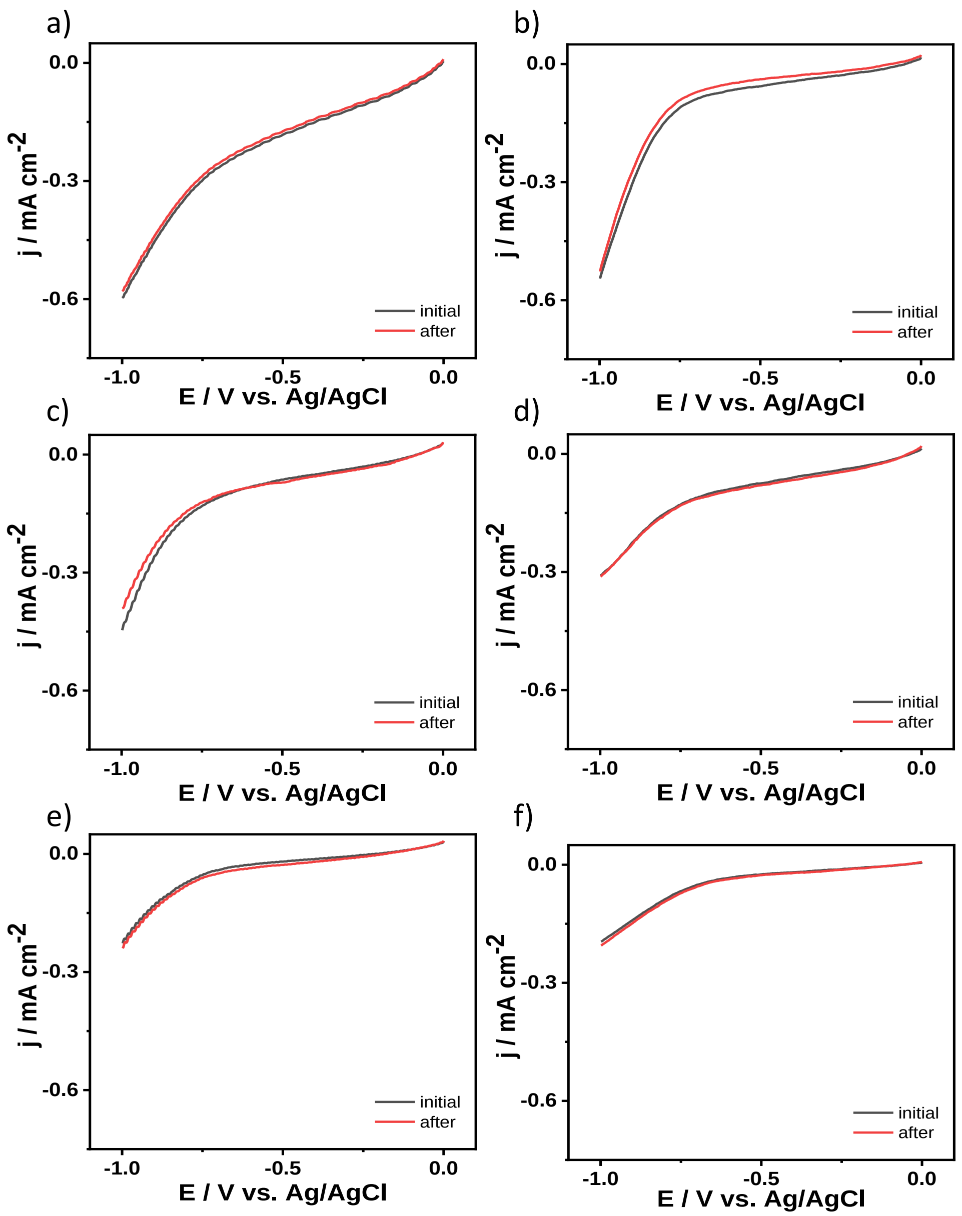

Figure 4.11: LSV initially and after the CO_2 reduction process for a) Pd-Cu/$Ti_3C_2T_x$ b) Pd-Co/$Ti_3C_2T_x$ c) Pd /$Ti_3C_2T_x$ d) Cu/$Ti_3C_2T_x$ e) Co/$Ti_3C_2T_x$ f) $Ti_3C_2T_x$.

The diameter of the semicircle provides co-agent evidence for the charge transfer resistance; thereby, Pd-Cu/$Ti_3C_2T_x$ and Pd-Co/$Ti_3C_2T_x$ revealed a lower value compared to mono doped Pd/$Ti_3C_2T_x$, Cu/$Ti_3C_2T_x$, Co/$Ti_3C_2T_x$, and $Ti_3C_2T_x$. This implies the superior interfacial electrolyte interface and a better electrochemical conductivity of Pd-Cu/$Ti_3C_2T_x$ and Pd-Co/$Ti_3C_2T_x$. To investigate the durability of the synthesized catalysts, the chronoamperometric test (I-T) was tested in CO_2-saturated 0.1 M $NaHCO_3$ for 10000 s at -1 V. Pd-Cu/$Ti_3C_2T_x$ revealed the greatest stability out of all the samples (Fig. 4.10 a). The liquid products were analyzed using ^{1}H NMR analysis. Pd-Cu/$Ti_3C_2T_x$, Pd-Co/$Ti_3C_2T_x$, and $Ti_3C_2T_x$ demonstrated the production of glucose, formate, and other C_3/C_2 (Fig. 4.10 b-d).

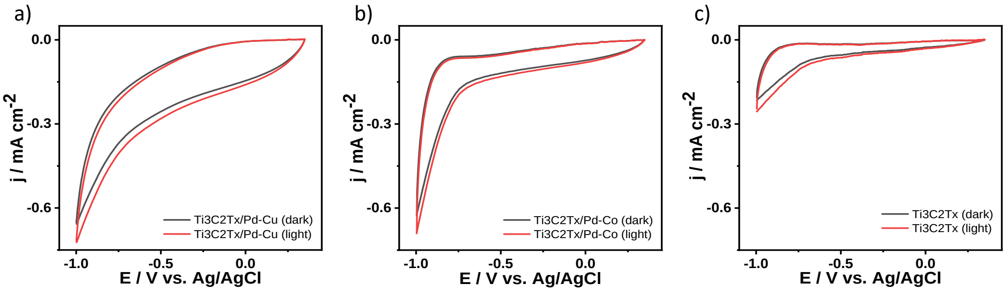

Figure 4.12: CV's for CO_2 reduction in dark and light for a) Pd-Cu/$Ti_3C_2T_x$ b) Pd-Co/$Ti_3C_2T_x$ c) $Ti_3C_2T_x$

Noticeably, Pd-Cu/$Ti_3C_2T_x$ is among the most efficient electrocatalysts for CO_2RR to formate in terms of FE, I_{CO_2RR}, and overpotential. Additionally, the obtained I_{CO_2RR} of Pd-Cu/$Ti_3C_2T_x$ was among the highest MXenes reported to date. The SEM after durability depicted the multilayered 2D sheets structure of Pd-Cu/$Ti_3C_2T_x$. Meanwhile, the EDX revealed the presence of Cu and Pd with very close atomic connections. This indicates the shape and composition stability of Pd-Cu/$Ti_3C_2T_x$ is in stable shape and composition of Pd-Cu/$Ti_3C_2T_x$ during the CO_2R.

For further invitation the stability of thus obtained materials, the LSV and CVs were measured after the I-T testes. However, prior to the measurements, a fresh electrolyte was used. Also, 50 cycles of CVs cleaning were carried out at (200 mV s^{-1}) under N_2 atmospheric in 0.1 M $NaHCO_3$ and then was measured at 50 mV s^{-1} for 3 cycles to measure the stability. The figure shows the LSVs measured after the I-T test, in which all materials revealed their initial voltammogram features obtained before the I-T testes. There are no detected anodic or cathodic peaks for any of the binary doped Pd-Cu and Pd-Co or the mono doped Pd, Cu, and Co metals, implying their stabilities inside $Ti_3C_2T_x$ lattice. Furthermore, all the as-prepared samples displayed more than 90% efficiency, including the metal-free $Ti_3C_2T_x$ (Fig. 4.10a-f).

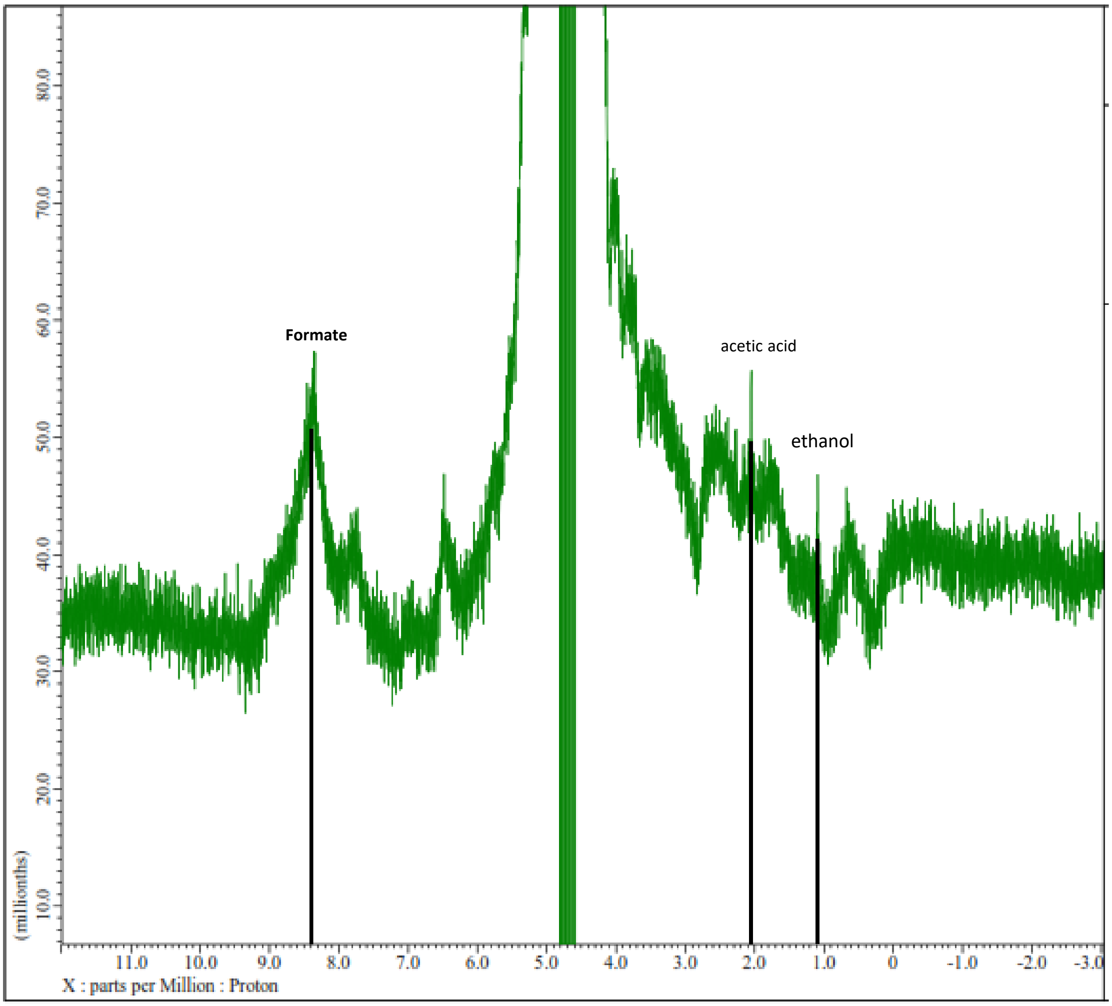

Figure 4.13: ^1H NMR analysis for the electrolyte using Pd-Co/$Ti_3C_2T_x$

All tested electrocatalysts showed a slight shift towards positive value in the CO_2RR potential, but metal-doped $Ti_3C_2T_x$ showed less shift compared to metal-free $Ti_3C_2T_x$. The shift in the CO_2RR potential of Pd-Cu/$Ti_3C_2T_x$ was lowest, indicating superior stability compared to the rest of the samples. This is due to the integration of Pd-Cu inside the stable Ti vacancies of $Ti_3C_2T_x$. Moreover, the photocatalytic behavior f the binary doped samples Pd-Cu and Pd-Co were investigated in comparison with the metal-free sample. While maintaining all the parameters used in the electrochemical reduction of CO_2, the cell was irradiated by the light from the solar simulator during the CV's of the samples. Both the binary doped and the undoped samples displayed almost the same increase in the current density (Fig. 4.12). Confirming that the material maintained its photo behavior which comes from the $Ti_3C_2T_x$, as despite the difference in the doped metals, the incrementation of the current was almost the same.

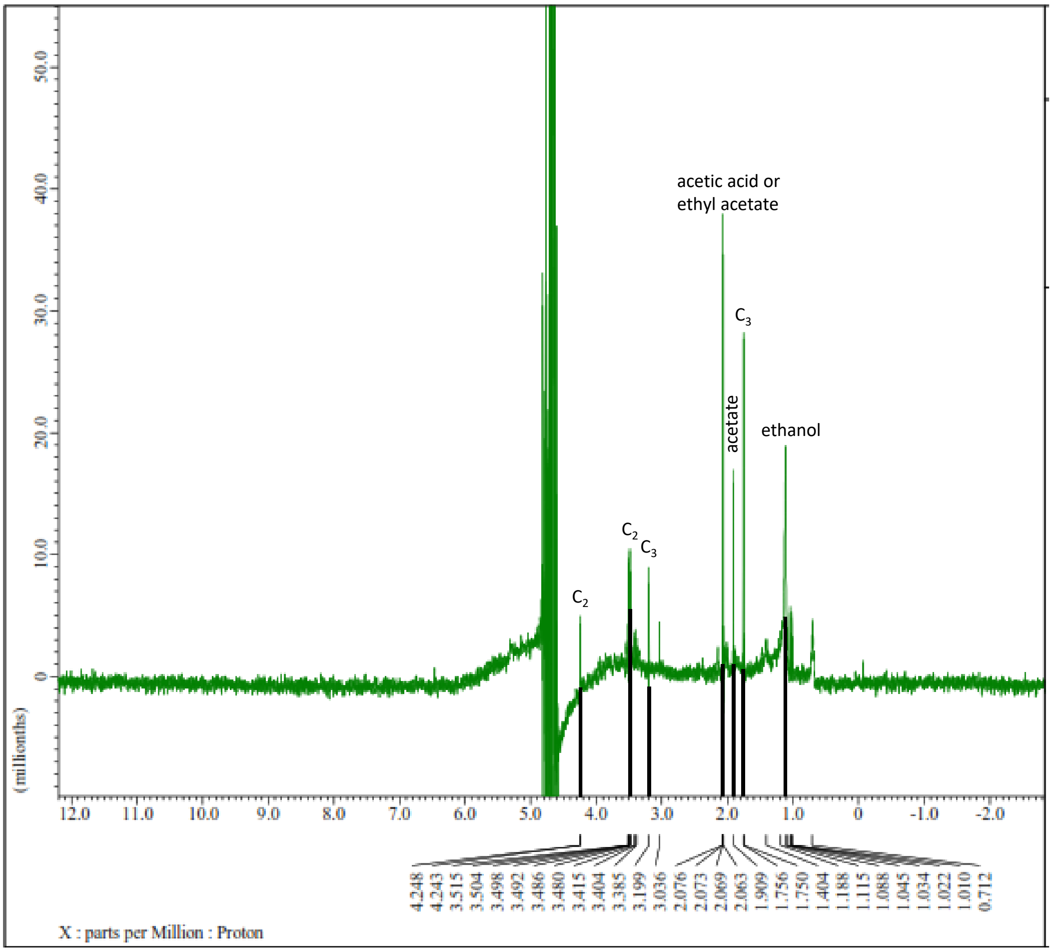

Figure 4.14: 1H NMR analysis for the electrolyte using Ti3C2Tx

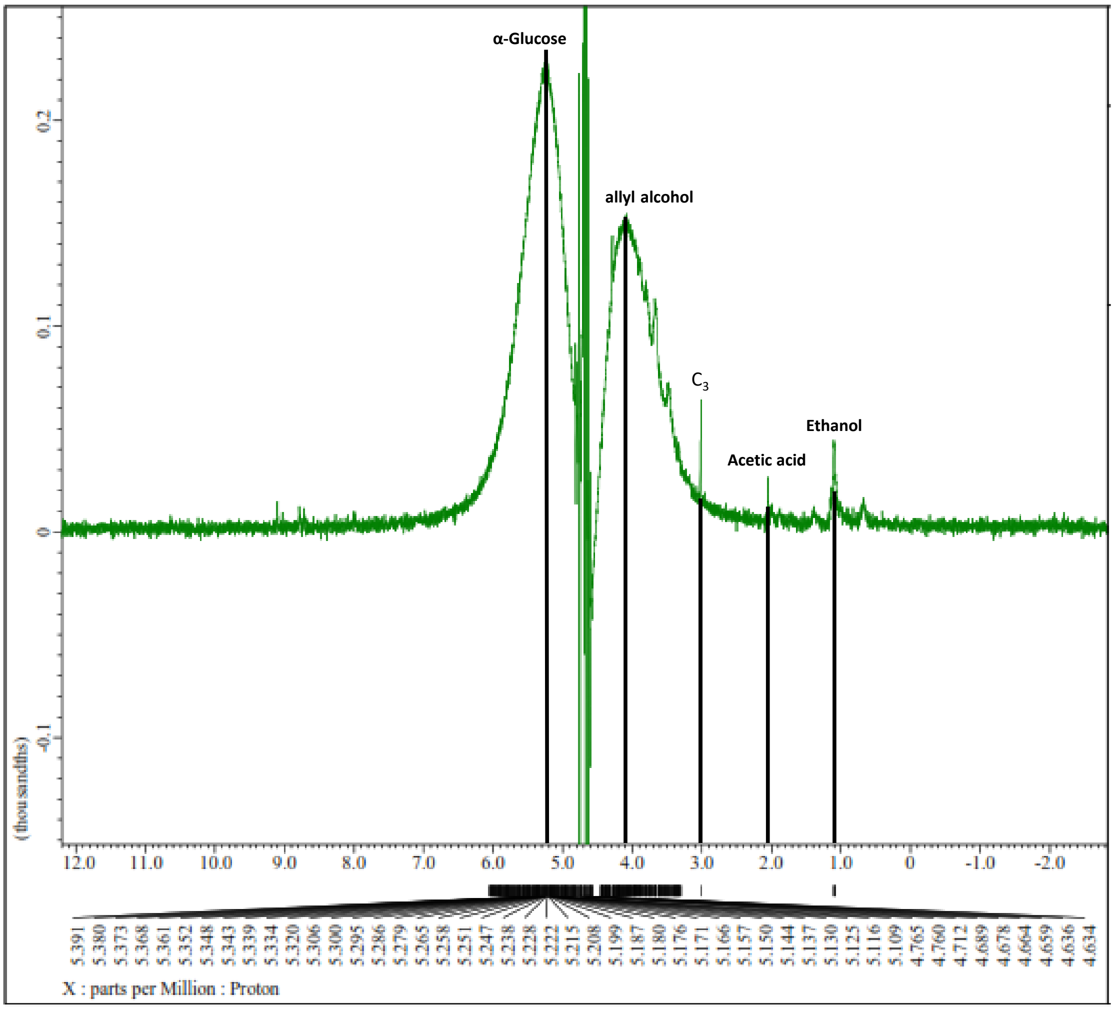

Figure 4.15: ^{1}H NMR analysis for the electrolyte using Pd-Cu/$Ti_3C_2T_x$

CO_2RR Mechanism:

The adsorption of CO_2 molecule and CO_2RR pathway and intermediates nearby or on the catalyst surface is the key factor for the selective formation of HCOOH and other products. The selective formation of HCOOH on Pd-Co/Ti_3C_2Tx (Fig. 4.13), as both PdCo and $Ti_3C_2T_x$ have weak adsorption ability for COOH (Fig. 4.14). Several studies suggested the formation of HCOOH via the initial generation of $CO_2^{\bullet-}$ radical anion nearby or weakly adsorbed on the surface of the catalyst. Thereby, the CO_2 molecule is initially adsorbed on the surface of the catalyst and one electron transferred to CO_2 to form $CO2^{\bullet-}$ radical anion, where C atom is available for hydrogenation in the presence of H_2O through the proton-coupled electron transfer (PCET) process, which results in the production of OCHO*and then protonation again to form HCOOH as the main product. The synergism between both Pd-Co and $Ti_3C_2T_x$, as well as their unique catalytic merits, precludes the H_2 proton reduction reaction during CO_2RR. However, due to the presence of the COOH* pathway cannot be circumvented to produce CH_3OH or CH_4 due to the presence of a catalyst with multiple metals (Pd & Co) as well as surface terminations (F, OH, and O) and dissimilar adsorption ability for the CO_2RR intermediates.

On the other hand, the CO_2 reduction reaction using Pd-Co/Ti_3C_2Tx follows the glyoxal mechanism. First, the CO_2 gas is adsorbed on the catalyst surface and activated by gaining an electron to form $CO_2^{\bullet-}$ radical anion. After that, the radical anion gained both an electron and a proton to form HCO2, followed by a hydrogenation step to form formaldehyde. However, unlike the Pd-Co doped sample, the Pd-Cu have a higher binding to HCOOH, resulting in gaining an electron to form HCO*. Thereafter two HCO* forms $C_2H_2O_2$followed by two PCET steps to finally generate $C_2H_4O_2$ (Fig. 4.14). It is worth noting that the overpotential for the electrochemical reduction of CO2 to formate and glucose is 0.39 and 0.68 eV VS SHE.

CHAPTER 5: CONCLUSION

In brief, two-dimensional $Ti_3C_2T_x$ nanosheets (T_x = O, OH, and F) doped atomically with Pd-Cu and Pd-Co (denoted as Pd-Cu/$Ti_3C_2T_x$ and Pd-Co/$Ti_3C_2T_x$) were synthesized by the selective chemical etching of Ti_3AlC_2 Max by HF and delamination by sonication followed by mixing with Cu precursor to allow the in-situ doping. This led to the formation of Pd-Cu/$Ti_3C_2T_x$ and Pd-Co/$Ti_3C_2T_x$ in uniform, exfoliated nanosheets, a high electrochemically active surface area (42 m^2g^{-1}), and coherently doped with Pd atoms (1.0 ± 1 Wt. %). The electrochemical CO_2 reduction activity and durability of the binary doped samples were substantially superior to $Ti_3C_2T_x$. Mainly, the current density of Pd-Cu/$Ti_3C_2T_x$ (-0.17 mA cm^{-2}) was 3.86 times higher than that of $Ti_3C_2T_x$ (-0.04 mA cm^{-2}) at the same potential. In addition, the CO_2 reduction potential on Pd-Cu/$Ti_3C_2T_x$ was substantially lower than that of $Ti_3C_2T_x$ by 0.06 V. Pd-Cu/$Ti_3C_2T_x$ successfully reduce CO_2 to form Glucose (47 %) as indicated by the ^{1}H NMR, whereas Pd-Co/$Ti_3C_2T_x$ successfully reduce CO_2 to form formate (55 %). The significant enhancement in the CO_2 reduction performance is ascribed to the combination between the inherent catalytic merits of Pd-M dopants (i.e., great electronic effect, CO* protonation, lower H_2 production ability, atomic dispersion, and stability against aggregation) and intrinsic physicochemical properties of $Ti_3C_2T_x$ (i.e., abundant adsorption sites, defects, and rich electron density). The current study may open new ways for the employment of $Ti_3C_2T_x$ doped with various dopants to control the selectivity of the hydrocarbon products for CO_2 reduction.

CHAPTER 5: REFERENCE

1. Han, N., et al., *CO2 Reduction: Promises of Main Group Metal–Based Nanostructured Materials for Electrochemical CO2 Reduction to Formate (Adv. Energy Mater. 11/2020).* Advanced Energy Materials, 2020. **10**(11): p. 2070046.
2. Kibria, M.G., et al., *Electrochemical CO2 reduction into chemical feedstocks: from mechanistic electrocatalysis models to system design.* Advanced Materials, 2019. **31**(31): p. 1807166.
3. Lv, F., et al., *Transition metal macrocycles for heterogeneous electrochemical CO2 reduction.* Coordination Chemistry Reviews, 2020. **422**: p. 213435.
4. Kondratenko, E.V., et al., *Status and perspectives of CO 2 conversion into fuels and chemicals by catalytic, photocatalytic and electrocatalytic processes.* Energy & environmental science, 2013. **6**(11): p. 3112-3135.
5. Kim, Y., et al., *Time-resolved observation of C–C coupling intermediates on Cu electrodes for selective electrochemical CO 2 reduction.* Energy & Environmental Science, 2020.
6. Hori, Y., et al., *Production of methane and ethylene in electrochemical reduction of carbon dioxide at copper electrode in aqueous hydrogencarbonate solution.* Chemistry Letters, 1986. **15**(6): p. 897-898.
7. Hori, Y. and A. Murata, *Electrochemical evidence of intermediate formation of adsorbed CO in cathodic reduction of CO2 at a nickel electrode.* Electrochimica Acta, 1990. **35**(11-12): p. 1777-1780.
8. Hori, Y., et al., *Electrocatalytic process of CO selectivity in electrochemical reduction of CO2 at metal electrodes in aqueous media.* Electrochimica Acta, 1994. **39**(11-12): p. 1833-1839.

9. Han, N., et al., *Promises of Main Group Metal–Based Nanostructured Materials for Electrochemical CO2 Reduction to Formate.* Advanced Energy Materials, 2020. **10**(11): p. 1902338.

10. Garg, S., et al., *Catalyst–Electrolyte Interactions in Aqueous Reline Solutions for Highly Selective Electrochemical CO2 Reduction.* ChemSusChem, 2020. **13**(2): p. 304-311.

11. Aresta, M., A. Dibenedetto, and A. Angelini, *Catalysis for the valorization of exhaust carbon: from CO2 to chemicals, materials, and fuels. Technological use of CO2.* Chemical reviews, 2014. **114**(3): p. 1709-1742.

12. Lu, X.-L., et al., *Carbon-based single-atom catalysts for CO 2 electroreduction: progress and optimization strategies.* Journal of Materials Chemistry A, 2020. **8**(21): p. 10695-10708.

13. Yang, H., et al., *Recent Progress in Self-Supported Catalysts for CO2 Electrochemical Reduction.* Small Methods, 2020: p. 1900826.

14. De Arquer, F.P.G., et al., *CO2 electrolysis to multicarbon products at activities greater than 1 A cm− 2.* Science, 2020. **367**(6478): p. 661-666.

15. Varela, A.S., W. Ju, and P. Strasser, *Molecular nitrogen–carbon catalysts, solid metal organic framework catalysts, and solid metal/nitrogen-doped carbon (MNC) catalysts for the electrochemical CO2 reduction.* Advanced Energy Materials, 2018. **8**(30): p. 1703614.

16. Hori, Y., K. Kikuchi, and S. Suzuki, *Production of CO and CH4 in electrochemical reduction of CO2 at metal electrodes in aqueous hydrogencarbonate solution.* Chemistry Letters, 1985. **14**(11): p. 1695-1698.

17. Johnson, T.C., D.J. Morris, and M. Wills, *Hydrogen generation from formic acid and alcohols using homogeneous catalysts.* Chemical Society Reviews,

2010. **39**(1): p. 81-88.

18. Ren, M., et al., *CO2 to Formic Acid Using Cu–Sn on Laser-Induced Graphene.* ACS Applied Materials & Interfaces, 2020. **12**(37): p. 41223-41229.

19. Kwon, I.S., et al., *Selective electrochemical reduction of carbon dioxide to formic acid using indium–zinc bimetallic nanocrystals.* Journal of Materials Chemistry A, 2019. **7**(40): p. 22879-22883.

20. Xie, H., et al., *Cu-based nanocatalysts for electrochemical reduction of CO2.* Nano Today, 2018. **21**: p. 41-54.

21. Dutta, A., et al., *Morphology matters: tuning the product distribution of CO2 electroreduction on oxide-derived Cu foam catalysts.* ACS Catalysis, 2016. **6**(6): p. 3804-3814.

22. Wang, Y., et al., *Catalyst synthesis under CO 2 electroreduction favours faceting and promotes renewable fuels electrosynthesis.* Nature Catalysis, 2020. **3**(2): p. 98-106.

23. Chou, T.-C., et al., *Controlling the oxidation state of the Cu electrode and reaction intermediates for electrochemical CO2 reduction to ethylene.* Journal of the American Chemical Society, 2020. **142**(6): p. 2857-2867.

24. Popović, S., et al., *Stability and degradation mechanisms of copper-based catalysts for electrochemical CO2 reduction.* Angewandte Chemie International Edition, 2020.

25. Martić, N., et al., *Paramelaconite-Enriched Copper-Based Material as an Efficient and Robust Catalyst for Electrochemical Carbon Dioxide Reduction.* Advanced energy materials, 2019. **9**(29): p. 1901228.

26. Wen, L., X. Wei-ping, and W. De-li, *Recent Progress in Copper-Based*

Catalysts for Electrochemical CO2 Reduction. Journal of Electrochemistry, 2019. **25**(4): p. 455.

27. Nitopi, S., et al., *Progress and perspectives of electrochemical CO2 reduction on copper in aqueous electrolyte.* Chemical reviews, 2019. **119**(12): p. 7610-7672.
28. Kuang, S., et al., *Stable Surface-Anchored Cu Nanocubes for CO2 Electroreduction to Ethylene.* ACS Applied Nano Materials, 2020.
29. Zhi, X., et al., *Selectivity roadmap for electrochemical CO2 reduction on copper-based alloy catalysts.* Nano Energy, 2020. **71**: p. 104601.
30. Arán-Ais, R.M., et al., *The role of in situ generated morphological motifs and Cu (i) species in C 2+ product selectivity during CO 2 pulsed electroreduction.* Nature Energy, 2020. **5**(4): p. 317-325.
31. Varela, A.S., et al., *Tuning the catalytic activity and selectivity of Cu for CO2 electroreduction in the presence of halides.* ACS Catalysis, 2016. **6**(4): p. 2136-2144.
32. Möller, T., et al., *Electrocatalytic CO2 Reduction on CuOx Nanocubes Tracking the Evolution of Chemical State, Geometric Structure, and Catalytic Selectivity using Operando Spectroscopy.* Angewandte Chemie, 2020.
33. Bagger, A., et al., *Electrochemical CO2 reduction: classifying Cu facets.* Acs Catalysis, 2019. **9**(9): p. 7894-7899.
34. Mistry, H., et al., *Highly selective plasma-activated copper catalysts for carbon dioxide reduction to ethylene.* Nature communications, 2016. **7**(1): p. 1-9.
35. Peterson, A.A., et al., *How copper catalyzes the electroreduction of carbon dioxide into hydrocarbon fuels.* Energy & Environmental Science, 2010. **3**(9):

p. 1311-1315.

36. Mori, K., et al., *Surface Engineering of a Supported PdAg Catalyst for Hydrogenation of CO2 to Formic Acid: Elucidating the Active Pd Atoms in Alloy Nanoparticles.* Journal of the American Chemical Society, 2018. **140**(28): p. 8902-8909.

37. Jiang, X., et al., *Bimetallic Pd–Cu catalysts for selective CO2 hydrogenation to methanol.* Applied Catalysis B: Environmental, 2015. **170-171**: p. 173-185.

38. Liu, L., et al., *Mechanistic Study of Pd–Cu Bimetallic Catalysts for Methanol Synthesis from CO2 Hydrogenation.* The Journal of Physical Chemistry C, 2017. **121**(47): p. 26287-26299.

39. Nie, X., et al., *Mechanistic Understanding of Alloy Effect and Water Promotion for Pd-Cu Bimetallic Catalysts in CO2 Hydrogenation to Methanol.* ACS Catalysis, 2018. **8**(6): p. 4873-4892.

40. Chen, H., et al., *Catalytic effect on CO2 electroreduction by hydroxyl-terminated two-dimensional MXenes.* ACS applied materials & interfaces, 2019. **11**(40): p. 36571-36579.

41. Li, N., et al., *Understanding of Electrochemical Mechanisms for CO2 Capture and Conversion into Hydrocarbon Fuels in Transition-Metal Carbides (MXenes).* ACS Nano, 2017. **11**(11): p. 10825-10833.

42. Handoko, A.D., et al., *Establishing new scaling relations on two-dimensional MXenes for CO 2 electroreduction.* Journal of Materials Chemistry A, 2018. **6**(44): p. 21885-21890.

43. Low, J., et al., *TiO2/MXene Ti3C2 composite with excellent photocatalytic CO2 reduction activity.* Journal of Catalysis, 2018. **361**: p. 255-266.

44. Qu, D., et al., *Nitrogen-doping and titanium vacancies synergistically promote*

CO2 fixation in seawater. Nanoscale, 2020.

45. Tahir, M. and B. Tahir, *2D/2D/2D O-C3N4/Bt/Ti3C2Tx heterojunction with novel MXene/clay multi-electron mediator for stimulating photo-induced CO2 reforming to CO and CH4*. Chemical Engineering Journal, 2020: p. 125868.

46. Tang, Q., et al., *Decorating g-C3N4 with alkalinized Ti3C2 MXene for promoted photocatalytic CO2 reduction performance*. Journal of Colloid and Interface Science, 2020. **564**: p. 406-417.

47. He, F., et al., *2D/2D/0D TiO2/C3N4/Ti3C2 MXene composite S-scheme photocatalyst with enhanced CO2 reduction activity*. Applied Catalysis B: Environmental, 2020: p. 119006.

48. Yang, C., et al., *2D/2D Ti3C2 MXene/g-C3N4 nanosheets heterojunction for high efficient CO2 reduction photocatalyst: Dual effects of urea*. Applied Catalysis B: Environmental, 2020. **268**: p. 118738.

49. Naguib, M., et al., *25th anniversary article: MXenes: a new family of two-dimensional materials*. Advanced materials, 2014. **26**(7): p. 992-1005.

50. Naguib, M., et al., *Two-dimensional nanocrystals produced by exfoliation of Ti3AlC2*. Advanced materials, 2011. **23**(37): p. 4248-4253.

51. Zhang, J., et al., *Scalable Manufacturing of Free-Standing, Strong Ti3C2Tx MXene Films with Outstanding Conductivity*. Advanced Materials, 2020: p. 2001093.

52. Handoko, A.D., S.N. Steinmann, and Z.W. Seh, *Theory-guided materials design: two-dimensional MXenes in electro-and photocatalysis*. Nanoscale Horizons, 2019. **4**(4): p. 809-827.

53. Chen, H., et al., *Defect-enhanced CO2 Reduction Catalytic Performance in O-terminated MXenes*. ChemSusChem, 2020.

54. Cao, S., et al., *2D/2D Heterojunction of Ultrathin MXene/Bi2WO6 Nanosheets for Improved Photocatalytic CO2 Reduction.* Advanced Functional Materials, 2018. **28**(21): p. 1800136.

55. Ye, M., et al., *Boosting the Photocatalytic Activity of P25 for Carbon Dioxide Reduction by using a Surface-Alkalinized Titanium Carbide MXene as Cocatalyst.* ChemSusChem, 2018. **11**(10): p. 1606-1611.

56. Chen, W., et al., *Ultrathin Co-Co LDHs nanosheets assembled vertically on MXene: 3D nanoarrays for boosted visible-light-driven CO2 reduction.* Chemical Engineering Journal, 2020. **391**: p. 123519.

57. Pan, A., et al., *CsPbBr3 Perovskite Nanocrystal Grown on MXene Nanosheets for Enhanced Photoelectric Detection and Photocatalytic CO2 Reduction.* The Journal of Physical Chemistry Letters, 2019. **10**(21): p. 6590-6597.

58. Xu, Y., et al., *Highly efficient photoelectrocatalytic reduction of CO 2 on the Ti 3 C 2/gC 3 N 4 heterojunction with rich Ti 3+ and pyri-N species.* Journal of Materials Chemistry A, 2018. **6**(31): p. 15213-15220.

59. Zeng, Z., et al., *Boosting the Photocatalytic Ability of Cu2O Nanowires for CO2 Conversion by MXene Quantum Dots.* Advanced Functional Materials, 2019. **29**(2): p. 1806500.

60. Handoko, A.D., et al., *Two-dimensional titanium and molybdenum carbide MXenes as electrocatalysts for CO2 reduction.* Iscience, 2020: p. 101181.

61. Yu, W., et al., *Direct Z-scheme g-C3N4/WO3 photocatalyst with atomically defined junction for H2 production.* Applied Catalysis B: Environmental, 2017. **219**: p. 693-704.

62. Low, J., et al., *Heterojunction Photocatalysts.* Advanced Materials, 2017. **29**(20): p. 1601694.

63. Nguyen, T.D.C., et al., *Novel photocatalytic conversion of CO2 by vanadium-doped tantalum nitride for valuable solar fuel production.* Journal of Catalysis, 2017. **352**: p. 67-74.

64. Ohkubo, K., et al., *Photocatalyses of Ru(II)–Re(I) binuclear complexes connected through two ethylene chains for CO2 reduction.* Journal of Catalysis, 2016. **343**: p. 278-289.

65. Ye, L., et al., *Thickness-ultrathin and bismuth-rich strategies for BiOBr to enhance photoreduction of CO2 into solar fuels.* Applied Catalysis B: Environmental, 2016. **187**: p. 281-290.

66. Sastre, F., et al., *Complete Photocatalytic Reduction of CO2 to Methane by H2 under Solar Light Irradiation.* Journal of the American Chemical Society, 2014. **136**(19): p. 6798-6801.

67. Wu, J.C.S., H.-M. Lin, and C.-L. Lai, *Photo reduction of CO2 to methanol using optical-fiber photoreactor.* Applied Catalysis A: General, 2005. **296**(2): p. 194-200.

68. Mora-Hernandez, J.M., A.M. Huerta-Flores, and L.M. Torres-Martínez, *Photoelectrocatalytic characterization of carbon-doped NaTaO3 applied in the photoreduction of CO2 towards the formaldehyde production.* Journal of CO2 Utilization, 2018. **27**: p. 179-187.

69. Cho, K.M., et al., *Amine-Functionalized Graphene/CdS Composite for Photocatalytic Reduction of CO2.* ACS Catalysis, 2017. **7**(10): p. 7064-7069.

70. Li, Q., et al., *CdS/Graphene Nanocomposite Photocatalysts.* Advanced Energy Materials, 2015. **5**(14): p. 1500010.

71. Shi, L., et al., *Electrostatic Self-Assembly of Nanosized Carbon Nitride Nanosheet onto a Zirconium Metal–Organic Framework for Enhanced*

Photocatalytic CO2 Reduction. Advanced Functional Materials, 2015. **25**(33): p. 5360-5367.

72. Ran, J., et al., *Earth-abundant cocatalysts for semiconductor-based photocatalytic water splitting.* Chemical Society Reviews, 2014. **43**(22): p. 7787-7812.

73. Lang, Q., et al., *High-index facet engineering of PtCu cocatalysts for superior photocatalytic reduction of CO2 to CH4.* Journal of Materials Chemistry A, 2017. **5**(14): p. 6686-6694.

74. Cao, S., et al., *Facet effect of Pd cocatalyst on photocatalytic CO2 reduction over g-C3N4.* Journal of Catalysis, 2017. **349**: p. 208-217.

75. Kar, P., et al., *Enhanced CH4 yield by photocatalytic CO2 reduction using TiO2 nanotube arrays grafted with Au, Ru, and ZnPd nanoparticles.* Nano Research, 2016. **9**(11): p. 3478-3493.

76. Hou, W. and S.B. Cronin, *A Review of Surface Plasmon Resonance-Enhanced Photocatalysis.* Advanced Functional Materials, 2013. **23**(13): p. 1612-1619.

77. Naguib, M., et al., *Two-Dimensional Nanocrystals Produced by Exfoliation of Ti3AlC2.* Advanced Materials, 2011. **23**(37): p. 4248-4253.

78. Han, X., et al., *2D Ultrathin MXene-Based Drug-Delivery Nanoplatform for Synergistic Photothermal Ablation and Chemotherapy of Cancer.* Advanced Healthcare Materials, 2018. **7**(9): p. 1701394.

79. Lipton, J., et al., *Mechanically strong and electrically conductive multilayer MXene nanocomposites.* Nanoscale, 2019. **11**(42): p. 20295-20300.

80. Kim, S.J., et al., *Metallic Ti3C2Tx MXene Gas Sensors with Ultrahigh Signal-to-Noise Ratio.* ACS Nano, 2018. **12**(2): p. 986-993.

81. Zhang, C., et al., *Microelectronics: Stamping of Flexible, Coplanar Micro-*

Supercapacitors Using MXene Inks (Adv. Funct. Mater. 9/2018). Advanced Functional Materials, 2018. **28**(9): p. 1870059.

82. Zhang, H., et al., *Preparation, mechanical and anti-friction performance of MXene/polymer composites.* Materials & Design, 2016. **92**: p. 682-689.

83. Wang, Y., et al., *Pt decorated Ti3C2 MXene for enhanced methanol oxidation reaction.* Ceramics International, 2019. **45**(2, Part A): p. 2411-2417.

84. Li, R., et al., *MXene Ti3C2: An Effective 2D Light-to-Heat Conversion Material.* ACS Nano, 2017. **11**(4): p. 3752-3759.

85. Ran, J., et al., *Ti3C2 MXene co-catalyst on metal sulfide photo-absorbers for enhanced visible-light photocatalytic hydrogen production.* Nature Communications, 2017. **8**(1): p. 13907.

86. Lin, H., et al., *Two-Dimensional Ultrathin MXene Ceramic Nanosheets for Photothermal Conversion.* Nano Letters, 2017. **17**(1): p. 384-391.

87. Low, J., et al., *Two-dimensional layered composite photocatalysts.* Chemical Communications, 2014. **50**(74): p. 10768-10777.

88. Ye, M., et al., *Boosting the Photocatalytic Activity of P25 for Carbon Dioxide Reduction by using a Surface-Alkalinized Titanium Carbide MXene as Cocatalyst.* ChemSusChem, 2018. **11**(10): p. 1606-1611.

89. Meng, X., et al., *Photocatalytic CO2 conversion over alkali modified TiO2 without loading noble metal cocatalyst.* Chemical Communications, 2014. **50**(78): p. 11517-11519.

90. Ouyang, S., et al., *Surface-Alkalinization-Induced Enhancement of Photocatalytic H2 Evolution over SrTiO3-Based Photocatalysts.* Journal of the American Chemical Society, 2012. **134**(4): p. 1974-1977.

91. Chang, X., T. Wang, and J. Gong, *CO2 photo-reduction: insights into CO2*

activation and reaction on surfaces of photocatalysts. Energy & Environmental Science, 2016. **9**(7): p. 2177-2196.

92. Liu, S., J. Xia, and J. Yu, *Amine-Functionalized Titanate Nanosheet-Assembled Yolk@Shell Microspheres for Efficient Cocatalyst-Free Visible-Light Photocatalytic CO2 Reduction.* ACS Applied Materials & Interfaces, 2015. **7**(15): p. 8166-8175.

93. Tu, W., et al., *Au@TiO2 yolk–shell hollow spheres for plasmon-induced photocatalytic reduction of CO2 to solar fuel via a local electromagnetic field.* Nanoscale, 2015. **7**(34): p. 14232-14236.

94. Manzanares, M., et al., *Engineering the TiO2 outermost layers using magnesium for carbon dioxide photoreduction.* Applied Catalysis B: Environmental, 2014. **150-151**: p. 57-62.

95. Yu, J., et al., *Enhanced Photocatalytic CO2-Reduction Activity of Anatase TiO2 by Coexposed {001} and {101} Facets.* Journal of the American Chemical Society, 2014. **136**(25): p. 8839-8842.

96. Jin, J., et al., *A Hierarchical Z-Scheme CdS–WO3 Photocatalyst with Enhanced CO2 Reduction Activity.* Small, 2015. **11**(39): p. 5262-5271.

97. Zhou, Y., et al., *High-Yield Synthesis of Ultrathin and Uniform Bi2WO6 Square Nanoplates Benefitting from Photocatalytic Reduction of CO2 into Renewable Hydrocarbon Fuel under Visible Light.* ACS Applied Materials & Interfaces, 2011. **3**(9): p. 3594-3601.

98. Wang, T., et al., *In situ synthesis of ordered mesoporous Co-doped TiO2 and its enhanced photocatalytic activity and selectivity for the reduction of CO2.* Journal of Materials Chemistry A, 2015. **3**(18): p. 9491-9501.

99. Wang, K., et al., *Sulfur-doped g-C3N4 with enhanced photocatalytic CO2-*

reduction performance. Applied Catalysis B: Environmental, 2015. **176-177**: p. 44-52.

100. Zhao, G., et al., *Co-porphyrin/carbon nitride hybrids for improved photocatalytic CO2 reduction under visible light.* Applied Catalysis B: Environmental, 2017. **200**: p. 141-149.

101. Gao, C., et al., *Co3O4 Hexagonal Platelets with Controllable Facets Enabling Highly Efficient Visible-Light Photocatalytic Reduction of CO2.* Advanced Materials, 2016. **28**(30): p. 6485-6490.

102. Ouyang, T., et al., *A Dinuclear Cobalt Cryptate as a Homogeneous Photocatalyst for Highly Selective and Efficient Visible-Light Driven CO2 Reduction to CO in CH3CN/H2O Solution.* Angewandte Chemie International Edition, 2017. **56**(3): p. 738-743.

103. Liu, D.-C., et al., *Highly efficient and selective visible-light driven CO2-to-CO conversion by a Co-based cryptate in H2O/CH3CN solution.* Chemical Communications, 2018. **54**(80): p. 11308-11311.

104. Wang, L., et al., *Hollow Multi-Shelled Structures of Co3O4 Dodecahedron with Unique Crystal Orientation for Enhanced Photocatalytic CO2 Reduction.* Journal of the American Chemical Society, 2019. **141**(6): p. 2238-2241.

105. Zhao, K., et al., *Metallic Cobalt–Carbon Composite as Recyclable and Robust Magnetic Photocatalyst for Efficient CO2 Reduction.* Small, 2018. **14**(33): p. 1800762.

106. Chen, W., et al., *MOFs-derived ultrathin holey Co3O4 nanosheets for enhanced visible light CO2 reduction.* Applied Catalysis B: Environmental, 2019. **244**: p. 996-1003.

107. Kumar, S., et al., *P25@CoAl layered double hydroxide heterojunction*

nanocomposites for CO2 photocatalytic reduction. Applied Catalysis B: Environmental, 2017. **209**: p. 394-404.

108. Wang, S., B.Y. Guan, and X.W. Lou, *Rationally designed hierarchical N-doped carbon@NiCo2O4 double-shelled nanoboxes for enhanced visible light CO2 reduction.* Energy & Environmental Science, 2018. **11**(2): p. 306-310.

109. Ou, M., et al., *Amino-Assisted Anchoring of CsPbBr3 Perovskite Quantum Dots on Porous g-C3N4 for Enhanced Photocatalytic CO2 Reduction.* Angewandte Chemie International Edition, 2018. **57**(41): p. 13570-13574.

110. Xu, Y.-F., et al., *Amorphous-TiO2-Encapsulated CsPbBr3 Nanocrystal Composite Photocatalyst with Enhanced Charge Separation and CO2 Fixation.* Advanced Materials Interfaces, 2018. **5**(22): p. 1801015.

111. Kong, Z.-C., et al., *Core@Shell CsPbBr3@Zeolitic Imidazolate Framework Nanocomposite for Efficient Photocatalytic CO2 Reduction.* ACS Energy Letters, 2018. **3**(11): p. 2656-2662.

112. Xu, Y.-F., et al., *A CsPbBr3 Perovskite Quantum Dot/Graphene Oxide Composite for Photocatalytic CO2 Reduction.* Journal of the American Chemical Society, 2017. **139**(16): p. 5660-5663.

113. Hou, J., et al., *Inorganic Colloidal Perovskite Quantum Dots for Robust Solar CO2 Reduction.* Chemistry – A European Journal, 2017. **23**(40): p. 9481-9485.

114. Wan, S., et al., *Perovskite-type CsPbBr3 quantum dots/UiO-66(NH2) nanojunction as efficient visible-light-driven photocatalyst for CO2 reduction.* Chemical Engineering Journal, 2019. **358**: p. 1287-1295.

115. Shen, J., et al., *Built-in electric field induced CeO2/Ti3C2-MXene Schottky-junction for coupled photocatalytic tetracycline degradation and CO2*

reduction. Ceramics International, 2019. **45**(18, Part A): p. 24146-24153.

116. Rahman, M.Z., K. Davey, and S.-Z. Qiao, *Carbon, nitrogen and phosphorus containing metal-free photocatalysts for hydrogen production: progress and challenges.* Journal of Materials Chemistry A, 2018. **6**(4): p. 1305-1322.

117. Han, C., et al., *Chainmail co-catalyst of NiO shell-encapsulated Ni for improving photocatalytic CO2 reduction over g-C3N4.* Journal of Materials Chemistry A, 2019. **7**(16): p. 9726-9735.

118. Fu, J., et al., *Hierarchical Porous O-Doped g-C3N4 with Enhanced Photocatalytic CO2 Reduction Activity.* Small, 2017. **13**(15): p. 1603938.

119. Wang, K., J. Fu, and Y. Zheng, *Insights into photocatalytic CO2 reduction on C3N4: Strategy of simultaneous B, K co-doping and enhancement by N vacancies.* Applied Catalysis B: Environmental, 2019. **254**: p. 270-282.

120. Zhang, X., et al., *Photocatalytic CO2 reduction over B4C/C3N4 with internal electric field under visible light irradiation.* Journal of Colloid and Interface Science, 2016. **464**: p. 89-95.

121. Thanh Truc, N.T., et al., *The superior photocatalytic activity of Nb doped TiO2/g-C3N4 direct Z-scheme system for efficient conversion of CO2 into valuable fuels.* Journal of Colloid and Interface Science, 2019. **540**: p. 1-8.

122. Hayat, A., et al., *Synthesis and optimization of the trimesic acid modified polymeric carbon nitride for enhanced photocatalytic reduction of CO2.* Journal of Colloid and Interface Science, 2019. **548**: p. 197-205.

123. Hong, J., et al., *Photocatalytic Reduction of Carbon Dioxide over Self-Assembled Carbon Nitride and Layered Double Hydroxide: The Role of Carbon Dioxide Enrichment.* ChemCatChem, 2014. **6**(8): p. 2315-2321.

124. Nie, N., et al., *Self-assembled hierarchical direct Z-scheme g-C3N4/ZnO*

microspheres with enhanced photocatalytic CO2 reduction performance. Applied Surface Science, 2018. **441**: p. 12-22.

125. Di, T., et al., *A direct Z-scheme g-C3N4/SnS2 photocatalyst with superior visible-light CO2 reduction performance.* Journal of Catalysis, 2017. **352**: p. 532-541.

126. Liu, S., et al., *Enhanced photocatalytic conversion of greenhouse gas CO2 into solar fuels over g-C3N4 nanotubes with decorated transparent ZIF-8 nanoclusters.* Applied Catalysis B: Environmental, 2017. **211**: p. 1-10.

127. Sun, Z., et al., *Enhanced CO2 photocatalytic reduction on alkali-decorated graphitic carbon nitride.* Applied Catalysis B: Environmental, 2017. **216**: p. 146-155.

128. Sun, Z., et al., *Enriching CO2 Activation Sites on Graphitic Carbon Nitride with Simultaneous Introduction of Electron-Transfer Promoters for Superior Photocatalytic CO2-to-Fuel Conversion.* Advanced Sustainable Systems, 2017. **1**(3-4): p. 1700003.

129. Xu, Y., et al., *Highly efficient photoelectrocatalytic reduction of CO2 on the Ti3C2/g-C3N4 heterojunction with rich Ti3+ and pyri-N species.* Journal of Materials Chemistry A, 2018. **6**(31): p. 15213-15220.

130. He, F., et al., *2D/2D/0D TiO2/C3N4/Ti3C2 MXene composite S-scheme photocatalyst with enhanced CO2 reduction activity.* Applied Catalysis B: Environmental, 2020. **272**: p. 119006.

131. Handoko, A.D., et al., *Two-Dimensional Titanium and Molybdenum Carbide MXenes as Electrocatalysts for CO2 Reduction.* iScience, 2020. **23**(6): p. 101181.

132. Zhang, X., et al., *Ti2CO2 MXene: a highly active and selective photocatalyst*

for CO2 reduction. Journal of Materials Chemistry A, 2017. **5**(25): p. 12899-12903.

133. Handoko, A.D., et al., *Establishing new scaling relations on two-dimensional MXenes for CO2 electroreduction.* Journal of Materials Chemistry A, 2018. **6**(44): p. 21885-21890.

134. Guo, Z., et al., *M2C-type MXenes: Promising catalysts for CO2 capture and reduction.* Applied Surface Science, 2020. **521**: p. 146436.

135. Xu, C., et al., *Large-area high-quality 2D ultrathin Mo2C superconducting crystals.* Nature Materials, 2015. **14**(11): p. 1135-1141.

136. Zhao, D., et al., *MXene (Ti3C2) vacancy-confined single-atom catalyst for efficient functionalization of CO2.* Journal of the American Chemical Society, 2019. **141**(9): p. 4086-4093.

137. Zhu, J., et al., *Composites of TiO2 nanoparticles deposited on Ti3C2 MXene nanosheets with enhanced electrochemical performance.* Journal of The Electrochemical Society, 2016. **163**(5): p. A785.

138. Peng, C., et al., *High efficiency photocatalytic hydrogen production over ternary Cu/TiO2@ Ti3C2Tx enabled by low-work-function 2D titanium carbide.* Nano Energy, 2018. **53**: p. 97-107.